NASA/TM—2013-216606 IEPC–2013–057

Farfield Plume Measurement and Analysis on the NASA-300M and NASA-300MS

Wensheng Huang, Rohit Shastry, George C. Soulas, and Hani Kamhawi
Glenn Research Center, Cleveland, Ohio

December 2013

NASA STI Program . . . in Profile

Since its founding, NASA has been dedicated to the advancement of aeronautics and space science. The NASA Scientific and Technical Information (STI) program plays a key part in helping NASA maintain this important role.

The NASA STI Program operates under the auspices of the Agency Chief Information Officer. It collects, organizes, provides for archiving, and disseminates NASA's STI. The NASA STI program provides access to the NASA Aeronautics and Space Database and its public interface, the NASA Technical Reports Server, thus providing one of the largest collections of aeronautical and space science STI in the world. Results are published in both non-NASA channels and by NASA in the NASA STI Report Series, which includes the following report types:

- TECHNICAL PUBLICATION. Reports of completed research or a major significant phase of research that present the results of NASA programs and include extensive data or theoretical analysis. Includes compilations of significant scientific and technical data and information deemed to be of continuing reference value. NASA counterpart of peer-reviewed formal professional papers but has less stringent limitations on manuscript length and extent of graphic presentations.

- TECHNICAL MEMORANDUM. Scientific and technical findings that are preliminary or of specialized interest, e.g., quick release reports, working papers, and bibliographies that contain minimal annotation. Does not contain extensive analysis.

- CONTRACTOR REPORT. Scientific and technical findings by NASA-sponsored contractors and grantees.

- CONFERENCE PUBLICATION. Collected papers from scientific and technical conferences, symposia, seminars, or other meetings sponsored or cosponsored by NASA.

- SPECIAL PUBLICATION. Scientific, technical, or historical information from NASA programs, projects, and missions, often concerned with subjects having substantial public interest.

- TECHNICAL TRANSLATION. English-language translations of foreign scientific and technical material pertinent to NASA's mission.

Specialized services also include creating custom thesauri, building customized databases, organizing and publishing research results.

For more information about the NASA STI program, see the following:

- Access the NASA STI program home page at *http://www.sti.nasa.gov*

- E-mail your question to *help@sti.nasa.gov*

- Fax your question to the NASA STI Information Desk at 443–757–5803

- Phone the NASA STI Information Desk at 443–757–5802

- Write to:
  STI Information Desk
  NASA Center for AeroSpace Information
  7115 Standard Drive
  Hanover, MD 21076–1320

NASA/TM—2013-216606 IEPC–2013–057

Farfield Plume Measurement and Analysis on the NASA-300M and NASA-300MS

Wensheng Huang, Rohit Shastry, George C. Soulas, and Hani Kamhawi
Glenn Research Center, Cleveland, Ohio

Prepared for the
33rd International Electric Propulsion Conference (IEPC2013)
sponsored by the Electric Rocket Propulsion Society
Washington, D.C., October 6–10, 2013

National Aeronautics and
Space Administration

Glenn Research Center
Cleveland, Ohio 44135

December 2013

Acknowledgments

We thank the following contributors: The NASA Space Technology Mission Directorate In-Space Propulsion project for funding this work, and Timothy D. Smith for managing the work; Peter Peterson for work on the design of the NASA-300M Hall thruster; Jonathan Van Noord of the University of Michigan and Ioannis G. Mikellides of the NASA Jet Propulsion Laboratory for work on the design of the NASA-300MS; Christopher Griffith for work on the design of both the NASA-300M and the NASA-300MS; Thomas Haag for work on the thrust stand and Daniel L. Brown and Joseph Blakely of the Air Force Research Laboratory for the retarding potential analyzer; and Kevin L. Blake, George W. Readus, George P. Jacynycz, and Thomas Raly for the thruster fabrication, assembly of the test setup, and operation of the vacuum facility.

Level of Review: This material has been technically reviewed by technical management.

Available from

NASA Center for Aerospace Information
7115 Standard Drive
Hanover, MD 21076–1320

National Technical Information Service
5301 Shawnee Road
Alexandria, VA 22312

Available electronically at http://www.sti.nasa.gov

Farfield Plume Measurement and Analysis on the NASA-300M and NASA-300MS

Wensheng Huang, Rohit Shastry, George C. Soulas, and Hani Kamhawi
National Aeronautics and Space Administration
Glenn Research Center
Cleveland, Ohio 44135

Abstract

NASA is developing a 10- to 15-kW Hall thruster system to support future NASA missions. This activity is funded under the Space Technology Mission Directorate Solar Electric Propulsion Technology Demonstration Mission project. As a part of the development process, the NASA-300M, a 20-kW Hall thruster, was modified to incorporate the magnetic shielding concept and named the NASA-300MS. This activity was undertaken to assess the viability of using the magnetic shielding concept on a high-power Hall thruster to greatly reduce discharge channel erosion. This paper reports on the study to characterize the far-field plumes of the NASA-300M and NASA-300MS. Diagnostics deployed included a polarly-swept Faraday probe, a Wien filter (ExB probe), a retarding potential analyzer, and a Langmuir probe. During the study, a new, more accurate, integration method for analyzing Wien filter probe data was implemented and effect of secondary electron emission on the Faraday probe data was treated. Comparison of the diagnostic results from the two thrusters showed that the magnetically shielded version performed with ~2 percent higher voltage utilization efficiency, ~2 percent lower plume divergence efficiency, and ~2 percent lower mass utilization efficiency compared to the baseline version. The net change in efficiency is within the aggregate measurement uncertainty so the overall performance is roughly equal for the two versions of the thruster. Anode efficiency calculated from thrust stand measurement corroborates this finding.

Abbreviations and Nomenclature

GRC	Glenn Research Center
HEFT	Human Exploration Framework Team
STMD	Space Technology Mission Directorate
AFRL	Air Force Research Laboratory
LEO	Low Earth Orbit
GEO	Geosynchronous Earth Orbit
300M	NASA-300M
300MS	NASA-300MS
300MS-2	NASA-300MS configuration 2
RPA	Retarding Potential Analyzer
CEX	Charge-exchange
SEE	Secondary Electron Emission
MCD	Mean Channel Diameter
η_a	Anode efficiency
η_v	Voltage utilization efficiency
η_d	Divergence efficiency
η_b	Current utilization efficiency
η_m	Mass utilization efficiency
η_q	Charge utilization efficiency

I. Introduction

In 2010, NASA established the Human Exploration Framework Team (HEFT) to analyze exploration and technology concepts and provided inputs to the agency's senior leadership on the key components of a safe, sustainable, affordable, and credible future human space exploration endeavor for the nation (Ref. 1). The team concluded, in part, that the use of a high power (i.e., on the order of 300 kW) solar electric propulsion system could significantly reduce the number of heavy lift launch vehicles required for a human mission to a near earth asteroid (Refs. 1 and 2). Hall thrusters were found to be ideal for such applications because of their high power processing capabilities and their efficient operation at moderate specific impulses, which leads to reduced trip times that are necessary for such missions (Refs. 2 to 4). Recent electric propulsion system model estimates that considered factors such as cost, mass, fault-tolerance, cost uncertainty, complexity, ground test vacuum facility limitations, previously demonstrated power capabilities, and possible technology limitations have shown that Hall thrusters operating at power levels of 20 to 50 kW are strong candidates for human exploration missions operating at total powers up to 500 kW (Refs. 2 and 5).

As an intermediate step towards the aforementioned higher power Hall thruster system, the Space Technology Mission Directorate (STMD) is investing in the development of a 10- to 15-kW Hall thruster. The NASA Glenn Research Center (GRC) is partnering with the Jet Propulsion Laboratory (JPL) to carry out this development work. The aforementioned thruster will serve as a stepping stone to higher power and provide a state-of-the-art propulsion system for the Solar Electric Propulsion Technology Demonstration Mission (SEP TDM). SEP TDM, initially announced in 2011, is aimed at demonstrating new cutting edge technology in flexible solar arrays, spacecraft bus, and electric propulsion that will increase the maturity of these SEP technologies for future commercial and government uses. Once these technologies have been demonstrated, they are expected to enable higher performance LEO to GEO transfers as well as a number of other near-Earth orbit transfers and station-keeping maneuvers. These technologies may also benefit a potential robotic mission to redirect an asteroid into cis-lunar orbit for crew exploration. In longer terms, these technologies will reduce mission costs for NASA interplanetary robotic missions in general, and will serve as a precursor to higher power systems for human interplanetary exploration.

The magnetic shielding (MS) concept, recently developed by JPL, has the potential to greatly reduce discharge channel wall erosion, which is a dominant life-limiting mechanism for traditional Hall thrusters (Ref. 6). This concept greatly benefits Hall thruster technology development and was previously demonstrated on a 6-kW Hall thruster (Refs. 7 and 8). To mitigate possible risks of applying the MS concept to higher power thrusters, NASA GRC and JPL took a combined experimental and modeling approach to study the application of the MS concept on the 20-kW NASA-300M. The NASA-300M was developed from 2004 to 2005 for project Prometheus but was not tested until recently due to project cancellation (Ref. 9). With the recent renewal in interest towards high-power Hall thrusters, the performance of the NASA-300M was characterized in 2010 (Ref. 9). The risk mitigation activities began with the modification of the NASA-300M into a magnetically-shielded version of the same thruster, called the NASA-300MS. A series of experiments and simulations were then performed to characterize the difference in behavior between the NASA-300M and the NASA-300MS. For a general overview of the MS modification, the system performance, and the simulation work, please see Kamhawi's paper (Ref. 10). For a description of the wall and interior Langmuir probe studies, please see Shastry's paper (Ref. 11). This paper will focus on the plume characterization study and the accompanying efficiency analysis.

The plume characterization study involved the use of a number of far-field diagnostics to study various plume characteristics of the NASA-300M and NASA-300MS. Measurements from these diagnostics can then be used to infer the effectiveness with which various performance-driving processes are carried out in the thrusters. Each of these processes is assigned an efficiency factor in a phenomenological efficiency model. By comparing the trends in the efficiency factors between the two thrusters, one can determine how applying the MS concept changes thruster performance and which

performance-driving processes are the drivers. For this study, a far-field Faraday probe was swept in a polar fashion to map the ion current density. A Wien filter, also known as an ExB probe, a retarding potential analyzer (RPA), and a Langmuir probe were mounted at a fixed location on the thruster axis in the far-field plume. The ExB probe, so called because of the orthogonal electric and magnetic fields inside the probe, was used to measure the species fractions of the various charged states of xenon. The RPA and the Langmuir probe were used to measure the energy per charge of the exhaust plume.

The main focus of this paper will be on the comparison of the efficiency analyses between the NASA-300M and NASA-300MS. This paper will also cover comparison between the NASA-300MS and NASA-300MS-2, which is the same as the NASA-300MS except with a shortened discharge channel. Other topics that will be covered include a new, more accurate, method of integration for analyzing ExB probe data and the effect of secondary electron emission on Faraday probe data.

The paper begins by describing the efficiency model used in the present study in Section II, followed by a description of the experiments in Section III. Next, the paper will describe data analyses and individual probe results for the RPA (Section IV), the ExB probe (Section V), and the Faraday probe (Section VI). Then, the paper presents the overall efficiency analyses and comparison between the 300M and 300MS, as well as the 300MS and 300MS-2, in Section VII. The paper ends with the conclusions in Section VIII. Appendices attached after Section VIII give the derivation of the new integration method for analyzing ExB data.

II. Background

The purpose of the present study is to determine what effects the application of the MS concept has on the performance of a high-power Hall thruster. The performance of a Hall thruster is typically measured by its anode efficiency, defined in Equation (1).

$$\eta_a = \frac{T^2}{2\dot{m}_a I_d V_d} \tag{1}$$

In this equation, T is thrust, $\dot{m}_a$ is anode mass flow rate, I_d is discharge current, and V_d is discharge voltage. However, the anode efficiency alone does not provide information about the plasma generation and acceleration processes that drive the performance of the thruster.

A phenomenological efficiency model is a way of breaking down and describing various physical phenomena that affect the overall efficiency of a Hall thruster. The purpose of a phenomenological efficiency model is to help researchers quantify the trends in the processes that drive the overall thruster efficiency. Many efficiency models have been proposed for the Hall thruster in the past. The complexity of these models depended on the operating environment and the state of knowledge in the community at the time. The model used in this paper is the same as a prior work by Shastry, (Ref. 12) which has evolved over time from a number of other studies (Refs. 13 to 16). The model is shown in Equations (2) to (7).

$$\eta_a = \eta_v \eta_d \eta_b \eta_m \eta_q \tag{2}$$

$$\eta_v = \frac{V_{RPA}}{V_d} \tag{3}$$

$$\eta_d = (\cos \delta)^2 \tag{4}$$

$$\eta_b = \frac{I_b}{I_d} \tag{5}$$

$$\eta_m = \left(\frac{m_{Xe} I_b}{\dot{m}_a e} \right) \alpha_m, \quad \alpha_m = \sum_k \frac{\Omega_k}{Z_k} \tag{6}$$

$$\eta_q = \frac{\left(\sum_k \Omega_k / \sqrt{Z_k} \right)^2}{\sum_k \Omega_k / Z_k} \tag{7}$$

Where η_a, the anode efficiency, is the same as that calculated from Equation (1), η_v is the voltage utilization efficiency, η_d is the divergence efficiency, η_b is current utilization efficiency, η_m is the mass utilization efficiency, η_q is the charge utilization efficiency, V_{RPA} is the ion energy per charge, δ is the charged-weighted divergence angle, the I_b is the total beam current, m_{Xe} is the mass of xenon, e is the elementary charge constant, α_m is the part of mass utilization efficiency that depends on charge state information, Ω_k is the current fraction of the k-th species, and Z_k is the charge of the k-th species.

The voltage utilization efficiency describes, on the average, how much of the voltage provided by the discharge supply is actually used to accelerate the ions. This factor is typically measured by the RPA.

The divergence efficiency describes how much of the kinetic energy imparted to the ions is axial, thrust-producing, kinetic energy. This factor is typically measured by the Faraday probe.

The current utilization efficiency describes how much of the discharge current is carried by ions instead of electrons. Electrons generate negligible thrust compared to the ions. This factor is typically measured by the Faraday probe.

The mass utilization efficiency describes how much of the mass flow exiting the thruster channel is in the form of ions. This factor typically requires data from the Faraday probe and the ExB probe.

The charge utilization efficiency is a number of terms representing the effects of having multiply-charged species that are not already described by the other terms in the efficiency model.

III. Experimental Setup

For the sake of brevity and to simplify plot labeling, NASA-300M will sometimes be referred to as the 300M in this paper. Similarly, 300MS is NASA-300MS and 300MS-2 is NASA-300MS-2. Operating conditions are labeled as www V, yy kW, where www is the discharge voltage in volts and yy is the discharge power in kilowatts. Unless otherwise noted, all spatial positions presented in this paper have been normalized by the mean channel diameter of the thrusters, which is identical for all three variants. The mean channel diameter (MCD) is defined as the average of the inner and outer discharge-channel wall diameters.

A. Thrusters and Test Matrices

The NASA-300M is a magnetic-layer Hall thruster. It was designed based on the principles outlined in Manzella's dissertation work (Ref. 17). This thruster was originally developed for high-specific-impulse missions (Ref. 9) and has lens-type magnetic field topology (Refs. 18 and 19). For this paper, the magnetic field settings of the 300M were optimized to give a shape roughly symmetric about the channel centerline while maximizing the anode efficiency. The NASA-300MS is a magnetically-shielded Hall thruster created from the NASA-300M. The magnetic circuit of the thruster was modified to achieve the MS topology while retaining most of the original 300M thruster. As such, the physical dimensions of the

300MS are nearly identical to that of the 300M. The biggest differences in the exterior of the two thrusters are the presence of chamfers on the downstream edge of the discharge channel walls. The physics-based modeling program Hall2De was used to validate the design of the magnetic field topology of the 300MS. For more details about the modifications needed to apply the MS concept and the modeling work, see Kamhawi's paper (Ref. 10). Experimental verification of the plasma potentials and electron temperatures at the channel walls was also performed and detailed in Shastry's paper (Ref. 11). For this paper, the magnetic field settings of the 300MS were set to maintain the MS topology while maximizing the anode efficiency. Both thrusters were operated with the same centrally-mounted hollow cathode, which was derived from the discharge cathode for NASA's Evolutionary Xenon Thruster (NEXT) (Ref. 9). The cathode flow fraction was 8 percent. Figures 1 and 2 show photographs of the NASA-300M and NASA-300MS, respectively.

The NASA-300MS-2 is a second configuration of the NASA-300MS with a shortened discharge channel. The modification was achieved by moving the anode downstream so that the channel length is roughly 20 percent shorter. This configuration was made to investigate whether the thruster could be made more compact to decrease mass without impacting the performance and magnetic shielding. The data will be used to guide the design of the 10- to 15-kW thruster. Comparisons will be made between the 300M and the 300MS to study the effect of applying magnetic shielding, and between the 300MS and the 300MS-2 to study the effect of shortening the discharge channel.

The nominal operating condition of NASA-300M and NASA-300MS is 500 V, 20 kW. For the purpose of comparing the thruster versions, eight operating conditions have been identified as reference points. These eight conditions span discharge voltages from 300 to 500 V, discharge currents from 20 to 50 A, and discharge powers from 10 to 20 kW. The thrusters operated with anode efficiencies of 65 to 70 percent over these eight conditions. Figure 3 shows the combined test matrix for the thruster versions. Reference points are highlighted by red circles and will be the main focus of the paper. Data from non-reference conditions will be used to supplement plots about trends within individual thruster versions. The boron nitride channel walls of the 300M have accumulated <110 hours of operation time prior to the start of this study. The boron nitride channel walls of the 300MS were freshly manufactured for this study.

The test campaign for the 300MS and 300MS-2 was spread over three tests. Test 1 was the performance and plume characterization test on the 300MS. Test 2 was the same but on the 300MS-2. Test 3 was the interior plasma characterization test on the 300MS. At the end of test 1, the boron nitride channel has seen 49 hours of operation. At the end of test 2, the channel has seen 82 hours of operation. At the end of test 3, the channel has seen 99 hours of operation. Figure 4 shows the 300MS prior to testing, after 49 hours of testing, and after 99 hours of testing. The discharge channels, especially at the downstream chamfers, are progressively darkened by deposited material. The data presented in this paper were obtained in tests 1 and 2. Details on test 3 are reported in Shastry's paper (Ref. 11).

Figure 1.—The NASA-300M on a thrust stand.

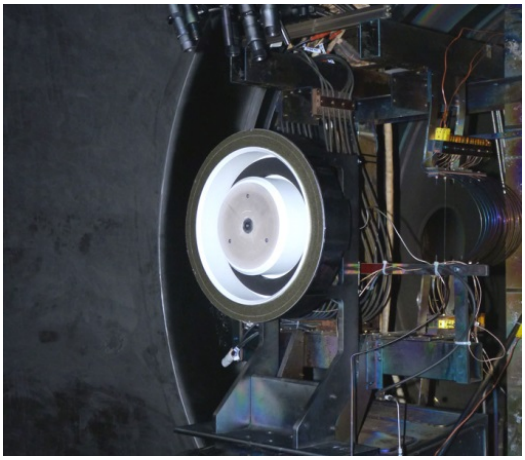

Figure 2.—The NASA-300MS on a thrust stand.

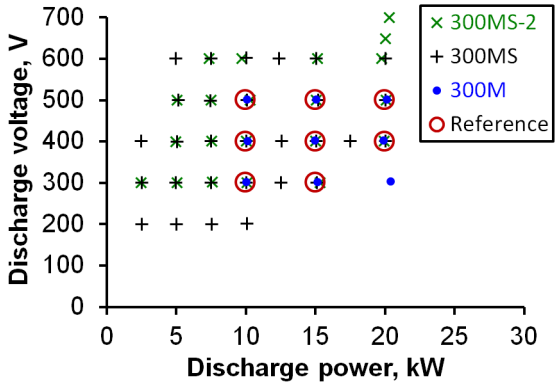

Figure 3.—The combined test matrix.

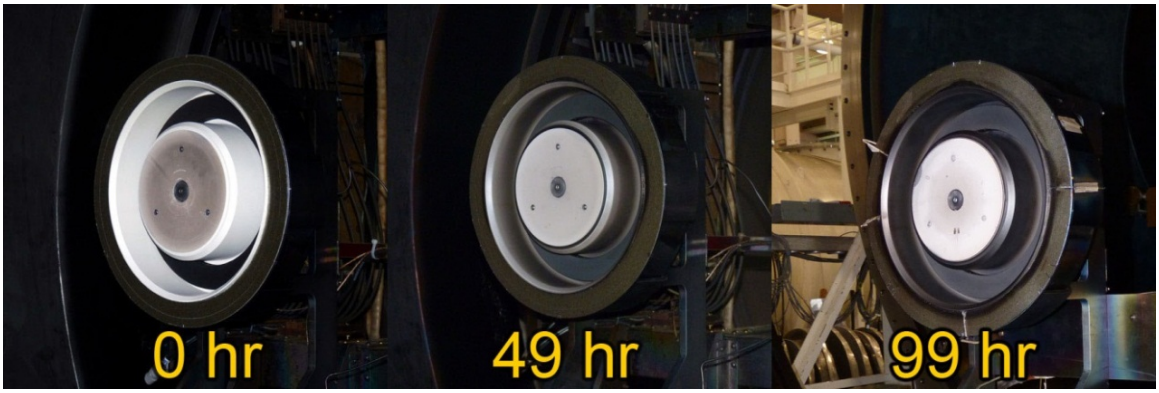

Figure 4.—NASA-300MS prior to test (left), after 49 hr of testing (middle), and after 99 hr of testing (right).

B. Test Facility

Testing was conducted in NASA GRC's Vacuum Facility 5. This cylindrical facility is 4.6 m in diameter and 18.3 m long and is pumped with a set of cryo-panels and 20 oil diffusion pumps. The thrusters were mounted on a thrust stand in the main volume of the vacuum facility to ensure low pressures near the thruster during operation. Facility pressures were monitored with one Pirani gauge and six ion gauges, one of which is mounted next to the thrust stand. Facility pressure uncertainties were estimated by the manufacturer to be within ±6 percent of reading. The pressure reading, corrected for xenon, next to the thrust stand was less than 3.5×10^{-3} Pa (2.6×10^{-5} torr) throughout testing.

A gas feed system made of commercially available components was used to feed xenon to the thruster. A 1000-sccm mass flow controller provides propellant to the anode while a 200-sccm controller provides propellant to the cathode. Both controllers were calibrated using xenon prior to testing. Typical uncertainty of measurement was ±1.0 percent of reading.

The commercial discharge power supply used is capable of supplying 2000 V at over 100 A with a 5.5 mF output filter capacitance. A 15.3 mF capacitor bank was connected in parallel with the power supply at the electrical feed-throughs of the vacuum facility to filter discharge current oscillations. In addition, separate commercial power supplies were used to power the cathode heater, cathode keeper, and electromagnets.

C. Thrust Stand and Plasma Diagnostics

This section will describe the thrust stand and the plasma diagnostics used to obtain data for the efficiency model. The plasma probes used in this study included a Langmuir probe, an RPA, an ExB probe, and a Faraday probe. Unless otherwise stated, all probe biases were applied with commercial power supplies.

The thrust stand used in this study is an inverted pendulum thrust stand designed by Haag (Ref. 20). It is actively cooled during operation. The nominal accuracy of this thrust stand is ±2 percent (Ref. 9). Long-term thermal drift is corrected by measuring the thrust signal with all gas flow to the thruster off and then assuming a linear change in the zero-thrust value over time. The maximum thermal drift was found to be ~10 mN.

A Langmuir probe, an RPA, and an ExB probe were mounted to a probe tower with accompanying shielding and shutters protecting the RPA and the ExB probe. This farfield probe tower was attached to a vertical motion stage located ~27 MCD downstream of the thruster exit plane and sitting behind a body shield. During the data acquisition process, each probe was moved vertically to a point roughly along the central axis of the thruster before measurements were taken. The probe tower retreated behind the shield once data acquisition was completed. Figure 5 shows a photograph of the diagnostics setup. Figure 6 shows a photograph of the farfield probe tower. A farfield Faraday probe was mounted onto a commercially available three-axis belt-driven motion system. The motion system provides 2D rectilinear motion and probe rotation. Positioning accuracy is ~1 mm and <0.1°, respectively.

For the test of the 300M, the Langmuir probe consists of a single tungsten wire protruding from an alumina tube. This probe was used to obtain the plasma potential at the same location as the RPA so that the RPA data can be corrected by this potential. For the tests of the 300MS, a disk probe was used to improve data fidelity. The Langmuir probe was swept at 10 Hz for 1 sec at each test point. The probe was connected to a custom circuit box where the probe current was passed through a shunt and the signal fed to an isolation amplifier. The bias voltage was passed through a voltage divider and fed to another isolation amplifier. Signal from the amplifiers were fed to a NI-9205 data acquisition module attached to a NI cDAQ-9178 unit.

For the test of the 300M, two four-grid RPAs were used to help validate a new RPA designed by the Air Force Research Laboratory (AFRL), courtesy of Daniel L. Brown and Joseph Blakely. The other RPA (just below the Langmuir probe in Fig. 6) was of GRC design and was known to not work well at closer than ~25 MCD for medium to high power Hall thruster testing. Results from the 300M test show that the two RPAs agree with each other. Furthermore, the AFRL RPA produced data with less noise and was

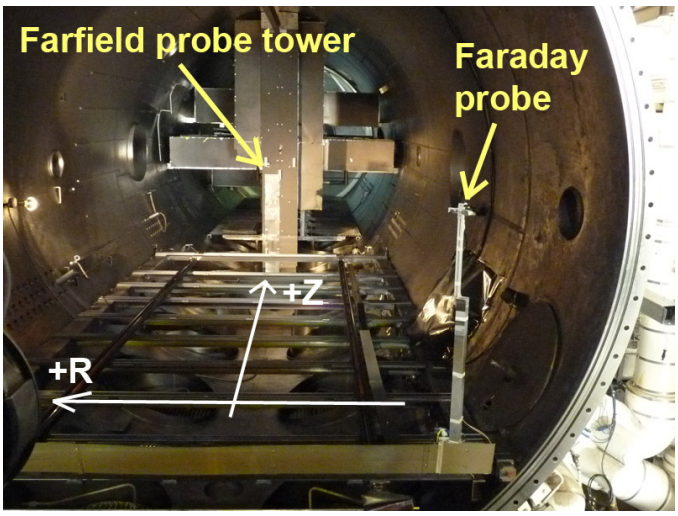

Figure 5.—Photograph of the diagnostics setup.

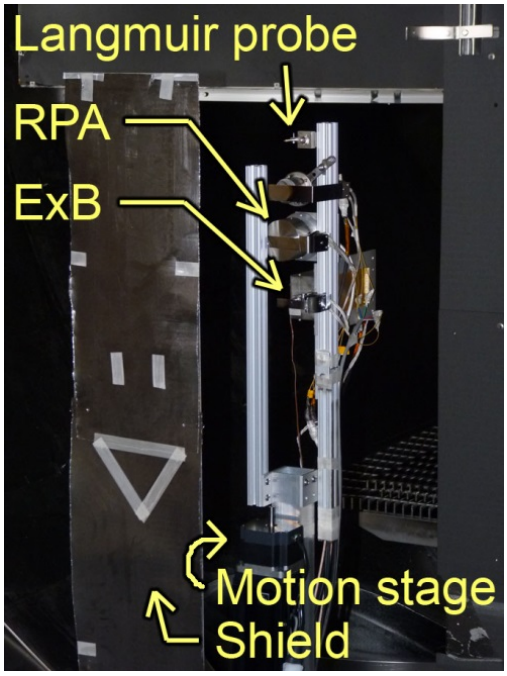

Figure 6.—Photograph of the farfield probe tower.

more resistant against plasma-induced breakdown. Only the AFRL RPA was used during the 300MS tests and all data presented in this paper are from the AFRL RPA. During testing, the electron suppression and repelling grids of the RPA was biased to –30 V with respect to facility ground while the ion retarding grid voltage was swept. The ion retarding grid was biased by a Keithley 2410 sourcemeter while the collected current was measured by a Keithley 6485 picoammeter.

The ExB probe is a commercial product of Plasma Controls, LLC. It was used to measure charged species current fraction. The ExB probe weights ~2 kg and is ~270 mm long. This ExB probe was the result of a Small Business Innovation Research project and has a proven history of usage (Ref. 15). Ions entering this ExB probe must first travel through a collimator, which ensures that the ions enter the ExB filter section along the probe axis. Perpendicular electric and magnetic fields in the filter section ensure that only charged particles of a given velocity can pass through to the electron suppression plate. There is a drift section between the filter section and the electron suppression plate which enhances probe resolution and makes sure bias on the suppression plate does not affect the filter section. The electron suppression plate has a small orifice through which ions can pass through. It was biased at –30 V with respect to facility ground to suppress secondary electron emission from the collector. Ions passing through the suppression plate were collected by the collector. The collimator used in this study has an entrance and exit orifice diameters of 0.76 mm. The bias plates that form the electric field in the filter section have a gap distance of 3 mm. The electron suppression plate orifice diameter is ~1.5 mm. The collector is large enough to collect all ions that pass through the electron suppression plate orifice. A thermocouple was attached to the case of this ExB probe to make sure it did not overheat and de-magnetize. During testing, the main bias plate voltage was swept by a Keithley 6487 picoammeter, which also measured the collector current.

The Faraday probe, which is of GRC design, was used to measure ion current density. Figure 7 shows a cross-sectional diagram of this Faraday probe. The collector area is a circle of diameter 17.39 mm. The front area of the collector is 238 mm^2. The probe has an overall diameter of ~28 mm. The collector and guard ring are made of molybdenum (to minimize secondary electron emission) and the insulating back is made of Macor. The collector and guard ring connections are mated to wires behind the insulating back and covered with fiberglass tape. The Faraday probe was set at 5 MCD away from the thruster because it needed to be far enough away from the thruster for the source of the thruster exhaust to be considered a point source. At the same time, the probe cannot be positioned much further away due to the effects of charge-exchange (CEX) and the physical size of the vacuum chamber. During each test, the probe was set to different bias voltages from –20 to –60 V in increments of 10 V with respect to ground. The bias was then set to the second most positive value that produces a consistent Faraday probe trace for recording data. This was done to ensure the electrons were properly repelled by the probe while keeping the sheath expansion negligible. Collected current was measured via a shunt and an isolation amplifier. The output of the amplifier was fed to another NI-9205 data acquisition module attached to the aforementioned NI cDAQ-9178 unit.

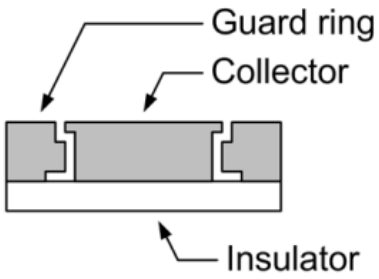

Figure 7.—Diagram of the farfield Faraday probe.

The experiment was conducted via a LabVIEW (National Instruments) program from a dedicated data acquisition computer. The motion stages were controlled by a motion controller that received movement commands from the computer. Encoder signals from the stages were fed into an encoder controller, which reports to the computer. The NI cDAQ-9178 data acquisition device and the various Keithley devices fed data to and were commanded by the computer. During the experiment, the computer automatically orchestrated the sequence of events that activated the various motion stages, shutters, and probes.

IV. Retarding Potential Analyzer Analysis

Data reduction was carried out in a specific sequence because, for the most part, each step of the analysis depended on the data obtained in the preceding steps. Though some of the analysis steps can be carried out independently, the accuracy of the result would have been decreased. For this study, the data analysis sequence was as follows, Langmuir probe analysis, RPA analysis, ExB probe analysis, and Faraday probe analysis. Additionally, pressure data is analyzed to help correct the ExB probe data for facility-background CEX effects. The data analysis as well as individual probe results will be covered in three analysis sections. The Langmuir probe and RPA analyses will be covered in this section. The ExB probe analysis will be covered in Section V. The Faraday probe analysis will be covered in Section VI. Differences between the presented data reduction procedures and traditional approaches will be highlighted with explanations for the rationale behind the new procedures.

A. Analysis Method

Langmuir probe analysis was carried out using simple Langmuir probe theory (Ref. 21). Since the Langmuir probe was swept at 10 Hz for 1 sec, 20 ramps were present in each data file. These data were averaged then smoothed using a Savitzky-Golay filter (Refs. 22 and 23). Then, the derivative of the probe current with respect to the probe voltage was plotted against the probe voltage. The voltage corresponding to the highest amplitude value on this plot is roughly equal to the plasma potential. This potential is needed to correct the RPA reading because the RPA ion retarding grid was biased with respect to the facility ground. The true filter voltage was equal to the ion retarding grid bias voltage minus the local plasma potential.

RPA analysis was carried out by first smoothing the RPA trace then taking the negative of the derivative of the collector current with respect to the bias voltage on the ion retarding grid. The result, plotted against the bias voltage, is proportional to the ion energy per charge distribution function (Ref. 24). Traditionally, the most probable voltage is taken as the average ion energy per charge. The most probable voltage is defined as the voltage where the amplitude of the plot maximizes. However, due to a combination of noise and broad ion distribution, the data can sometimes contain small bumps on top of the main population that skewed the location of the most probable voltage. To deal with this issue, the average ion energy per charge was calculated via ensemble-averaging using only the part of the trace where the amplitude exceeded half of the maximum amplitude. This averaging approach will be referred to as the threshold-based averaging approach with a 50 percent threshold. For clean traces, this approach yield values that are at most 3 to 4 V different from the most probable voltage. For noisy traces, this approach yield values that are insensitive to noise spikes. Figure 8 shows plots from applying the threshold-based averaging approach to a slightly noisy RPA trace. The black dashed vertical line indicates the location of the most probable voltage, the red solid vertical line indicates the result of using the threshold-based averaging approach with the 50 percent threshold, and the red dashed horizontal line indicates the 50 percent of maximum threshold.

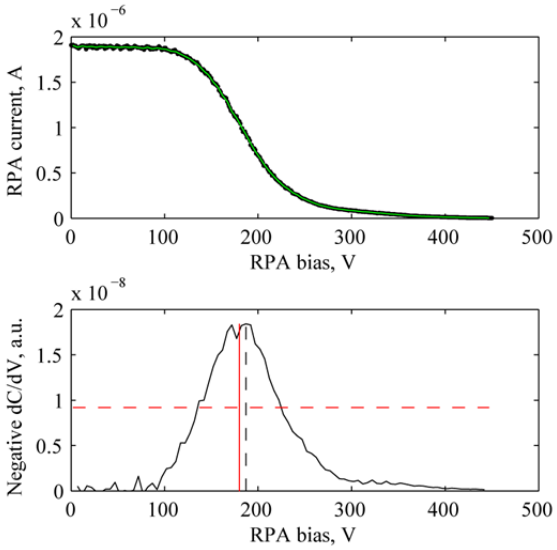

Figure 8.—Sample RPA analysis plots.

Note that in theory the most accurate result is obtained by ensemble-averaging the entire RPA trace. However, doing so often produces unphysical results because the ion energy per charge distribution as measured by the RPA is typically much broader than the real distribution due to the wide acceptance angle of the RPA. This is also the reason the traditional approach relies on the most probable voltage. Using the 50 percent threshold-based ensemble-averaging approach essentially strikes a balance between excluding broadened data and maintaining some degree of noise insensitivity.

A full uncertainty analysis will not be carried out for every element of this study. Only uncertainties associated with novel parts of the study and uncertainties that are dominant will be analyzed. The uncertainty in the voltage utilization as calculated from Equation (3) is ~1 percent. This uncertainty is a combination of the uncertainty in the RPA analysis method and the Langmuir probe analysis method used to correct the RPA measurement.

B. RPA and Langmuir Probe Results and Comparisons

Figure 9 shows example RPA traces from the same reference point (400 V, 20 kW) for the 300M and 300MS. This figure illustrates a common trend seen in the RPA data; the distributions appear to be wider with a longer and fatter energy tail for the 300MS than for the 300M. Note that the distributions derived from the RPA are broadened by the somewhat poor resolution of the probe, which has a tendency to wash out differences between the thrusters. Thus, the real differences between the energy distribution functions of the 300M and 300MS are expected to be greater than indicated by the RPA and are difficult to quantify.

Table 1 summarizes the results of the RPA and Langmuir probe analyses for all three thruster versions across the eight reference points. At the bottom of the table, the average and standard deviation of the voltage utilization efficiency across the eight reference points are shown. The averages show, more clearly, the differences in values between the three thruster versions. The standard deviations give indications of the spread in values across the eight reference points. By comparing the standard deviations, one can get a sense of whether the spread changes with thruster versions, which may indicate a change in thruster physics. A change in spread can also indicate a change in the noise environment of the probe. Thus, care should be taken when interpreting the standard deviation, especially if the amplitude of the difference is lower than the uncertainty of the probe data. From Table 1, one can see that the three thruster versions behave largely the same in terms of voltage utilization. Both versions of the 300MS perform slightly better than the 300M.

TABLE 1.—SUMMARY OF VOLTAGE UTILIZATION ANALYSIS

		Plasma potential, V			Energy per charge, V			Voltage utilization efficiency		
Disch. voltage, V	Disch. power, kW	300M	300MS	300MS-2	300M	300MS	300MS-2	300M	300MS	300MS-2
300	10	6.3	7.6	7.2	278	285	288	0.926	0.947	0.957
300	15	6.3	6.4	7.0	281	281	291	0.934	0.935	0.969
400	10	6.9	7.7	8.0	377	389	395	0.942	0.972	0.984
400	15	7.4	7.7	8.1	377	385	391	0.940	0.961	0.978
400	20	6.9	7.2	7.2	378	390	396	0.943	0.974	0.987
500	10	6.9	8.1	7.6	481	473	484	0.962	0.946	0.968
500	15	7.9	8.1	8.1	472	491	491	0.942	0.980	0.982
500	20	7.9	8.1	7.8	480	491	496	0.959	0.981	0.992
	Average:	----	----	----	----	----	----	0.944	0.962	0.977
	Std. dev.:	----	----	----	----	----	----	0.012	0.017	0.012

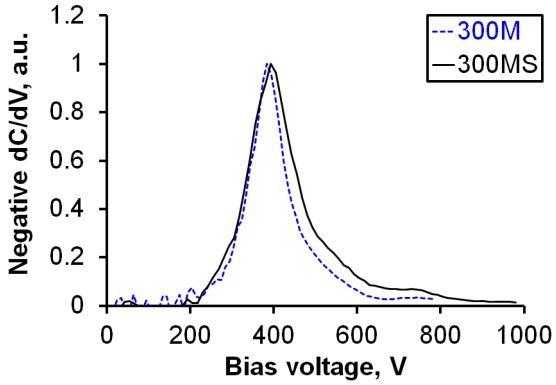

Figure 9.—Comparison of ion energy-per-charge distributions for the 300M and 300MS at 400 V, 20 kW.

Note that some values of energy per charge for the 300MS and 300MS-2 are very close to the discharge voltage and seem physically impossible at first glance given that some ~10 V of the discharge voltage must be used to extract electrons from the cathode. However, one should keep in mind that the total possible voltage drop from anode to cathode actually includes the drop across the anode sheath. Thus the true maximum total voltage drop is slightly higher than the discharge voltage. While accounting for the anode sheath voltage is interesting, this quantity is not easy to measure. The total discharge power is still easiest to calculate by using the discharge voltage with the discharge current so the efficiency model presented here uses the discharge voltage to calculate voltage utilization.

V. ExB Probe Analysis

A. Analysis Method

The ExB probe is used as a velocity filter for charged species spectrometry. Since different charged species are accelerated to different velocities by going through roughly the same potential drop, they will show up as different peaks when interrogated by the ExB probe. For a scenario where the ExB probe velocity resolution is at least several times smaller than the width of the ion velocity distribution function (VDF), the preferred method for analyzing ExB probe data is via integration. In the past, most integration schemes involved fitting some general distribution equation form to the ExB probe trace and calculating either by geometry or by numerical integration the area under the curve (Refs. 12, 25, and 26). This is

done because the ion distributions from different charged species tend to overlap in the regions between peaks, making a direct integration of only one species at a time impossible without some kind of assumption on the form of the distribution. The domain of the curve-fit for each species usually needs to be bounded such that only the current signal generated by one species is being fitted at a time.

In the process of carrying out the present study, the area under the curve was discovered to not be exactly proportional to the current associated with each species. A new set of integration formulas were derived from scratch for the purpose of analyzing ExB probe data. The results of the new derivation closely matches the derivation by Kim (Ref. 27), though Kim did not publish the species fraction formulas and did not try to calculate the current fraction (that was not his objective). As such, the new derivation continues where Kim's work left off.

Note that Kim's work (Ref. 27) is the first published instance where the ExB probe was used to study a Hall thruster and strongly influenced all subsequent work in this area including all other cited work on ExB probe studies.

Full derivation of the new integration formulas for analyzing ExB probe data is presented in Appendix A. Additional mathematical comparisons between the traditional and new integration formulas are shown in Appendix B. The ExB probe data presented in this paper are analyzed using the following steps.

In the first step, one begins by selecting a form for the VDF. A number of different VDF forms were tried including the triangle, similar to what was proposed by Beal (Ref. 25), the Gaussian, first proposed by Linnell (Ref. 26), and the variable exponential, first proposed by Kim (Ref. 27). Two additional forms were also tried for this study: the twin Gaussian and skew-normal distributions. Equations (8) to (12) show the mathematical forms of VDFs that were tried in the present study. They are, in order, triangle, Gaussian, variable exponent, twin Gaussian, and skew-normal.

$$\text{Triangle: } f_j(u) = \begin{cases} (-a/b)*|u-c|+a, & c-b<u<c+b \\ 0, & \text{else} \end{cases} \tag{8}$$

$$\text{Gaussian: } f_j(u) = a*\exp[-b(u-c)^2] \tag{9}$$

$$\text{Variable Exponent: } f_j(u) = a*\exp[-b|u-c|^n] \tag{10}$$

$$\text{Twin Gaussian: } f_j(u) = a_1*\exp[-b_1(u-c_1)^2] + a_2*\exp[-b_2(u-c_2)^2] \tag{11}$$

$$\text{Skew-Normal: } f_j(u) = a*\exp\left[-\frac{(u-c)^2}{2b^2}\right]*\left\{1+\text{erf}\left[-\frac{d*(u-c)}{\sqrt{2b^2}}\right]\right\} \tag{12}$$

Where a, b, c, d, n, a_1, b_1, c_1, a_2, b_2, and c_2, are fitting constants. The term erf[] refers to the error function. The twin Gaussian and the skew-normal forms were tried in an attempt to capture the tail that is often observed in the VDFs of accelerated ions in a Hall thruster. In particular, the twin Gaussian form generally gives much better fits to the data than any other form. However, it can generate erroneous results if the curve-fit boundary is not properly chosen. For instance, if the boundary includes peaks from two different species, the computer will fit the twin Gaussian form to both peaks and treat them as a single species. Analysis of the 300M ExB probe data, which show relatively little overlap between neighboring peaks, showed that while the twin Gaussian form fitted very well, it did not generate results that were much different from the other forms. This behavior suggests that properly capturing the width and height of the distribution was sufficient to obtain accurate results in the absence of strong overlap.

Unfortunately, the 300MS ExB probe data showed strong overlap between neighboring peaks, and the cause was hypothesized to be a combination of wide VDFs and large high-velocity tails (Fig. 9). The use of the skew-normal distribution was an attempt to obtain useful data despite the strong overlap between peaks. Compared to a normal distribution, the skew-normal distribution has an additional parameter that controls skewness and collapses into a normal distribution when that parameter is equal to 0. The skew-normal distribution retains the general shape of the normal distribution but has skewness. Note the Gaussian is essentially a normal distribution. Skew-normal was chosen as the VDF form to use for the present study because the associated efficiency analysis results were the most consistent across all three thruster versions.

In the second step, the selected VDF form is inserted into Equation (13)

$$I_{P,j}(V_P) = K_1 n_j V_P^{\,3} f_j\left(\frac{V_P}{B_0 D_f}\right) \sim V_P^{\,3} f_j(V_P) \tag{13}$$

Where $I_{P,j}$ is the contribution of the j-th species to the ExB probe collector current, n_j is the number density of the j-th species, V_P is the ExB probe bias, B_0 is the magnetic field magnitude in the ExB filter section, and D_f is the gap between ExB bias plates. K_1 is a constant that will be derived in Appendix A. In practice, K_1, n_j, B_0, and D_f are constant with respect to the bias voltage and can be rolled into the fitting constants of the VDF forms. Curve-fits are then performed using Equation (13) for each charged species in the ExB probe data in order to obtain the values of the various fitting constants.

For this study, the curve-fit process starts with the singly-charged species peak. The fitted curve is then subtracted out of the data and the remainder is curve fitted for the doubly-charged species peak. The process is repeated until the quadruply-charged species peak is fitted. Boundaries are used to make sure the curve-fit is performed over domains that are dominated by only one charged species at a time. For each species, the left boundary is set to 0.667 times the voltage location of the corresponding species peak; the right boundary is set to halfway between the peak location of this species and the peak location of the next higher charged species.

The voltage location of the singly-charged species is first manually determined from many ExB probe traces. A second-order polynomial fit of this location against the discharge voltage was performed and found to have an R-squared value of 0.995. The ratio of the locations of the remaining peaks to the location of the singly-charged peak is assumed to be constant and found by manually studying several ExB probe traces. The analysis code then uses the discharge voltage, the second-order polynomial fit, and the peak location ratios to predict the location where each charged species should be located. For ExB probe traces with distinguishable peaks, visual inspection of the curve-fit process shows the code accurately predicts the peak locations.

Figure 10 shows a set of analysis plots generated by the program that performs the ExB probe analysis. The thruster is the 300M and the operating condition is 500 V, 20 kW. For convenience, the paper will refer to the six subplots in order from left to right, top to bottom as (a) to (f). Subplot (a) shows the raw ExB probe data as black data points with red dashed vertical lines showing the location of the first four peaks. Subplots (b), (c), (e), and (f) show the four sub-steps in the curve-fitting process. The program fits the appropriate equation to the 1st peak, subtracts the fitted data, then fits the 2nd peak, and so on. The data prior to the fit at each curve-fit sub-step is shown as black dots, the red solid line shows the curve-fit, the magenta dashed vertical lines show the curve-fit boundaries, and the blue dashed line shows the leftover result after subtraction. Subplot (d) shows the raw data in black dots with a red solid line that represents the sum of all four curve-fit sub-steps super-imposed on top. Figure 11 shows the same for the 300MS.

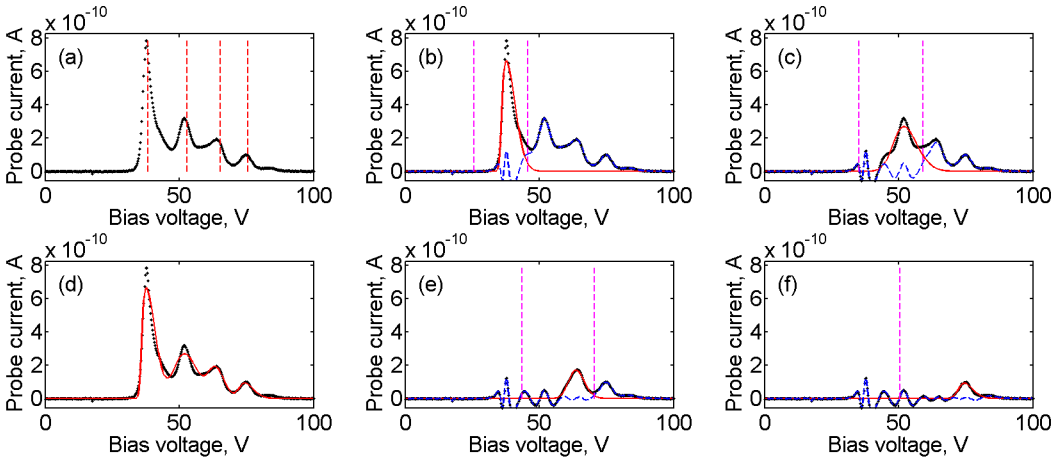

Figure 10.—ExB probe analysis plots for the 300M operating at 500 V, 20 kW.

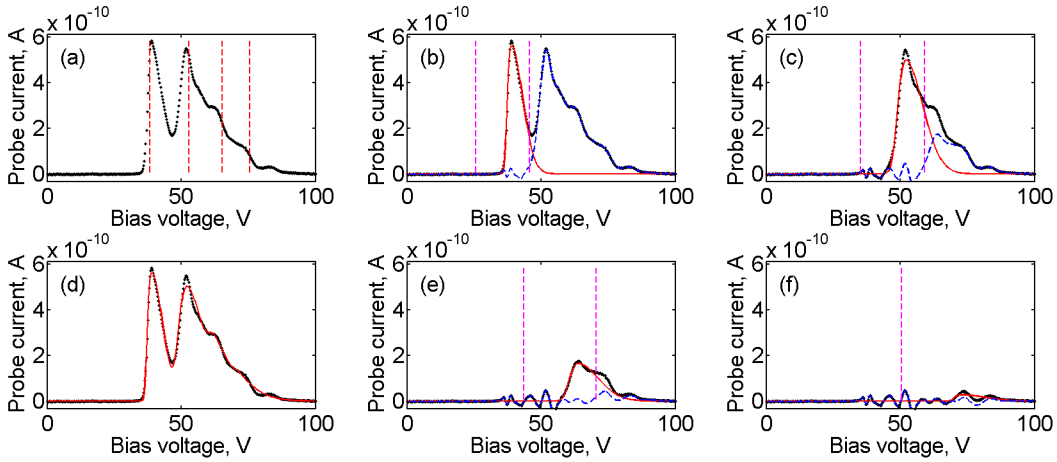

Figure 11.—ExB probe analysis plots for the 300MS operating at 500 V, 20 kW.

In the third step, the $I_{P,j}$ of all the species are substituted into Equations (14) and (15) to calculate the species and current fractions, respectively,

$$\zeta_j \equiv \frac{n_j}{\sum_k n_k} = \frac{\int_0^\infty \frac{I_{P,j}(V_P)}{V_P{}^3} dV_P}{\sum_k \int_0^\infty \frac{I_{P,k}(V_P)}{V_P{}^3} dV_P} \tag{14}$$

$$\Omega_j \equiv \frac{I_j}{\sum_k I_k} = \frac{Z_j \int_0^\infty \frac{I_{P,j}(V_P)}{V_P{}^2} dV_P}{\sum_k Z_k \int_0^\infty \frac{I_{P,k}(V_P)}{V_P{}^2} dV_P} \tag{15}$$

Where I_j is the current contributed by the j-th species at the entrance of the ExB probe collimator. Since the entrance orifice area is a constant across all I_j's, I_j and I_k can be replaced with the corresponding current densities. Note that I_j is not the same as $I_{P,j}$, which is current at the collector of the ExB probe. In this study, Xe^{4+} was not accounted for in the current and species fraction calculation because those typically comprise less than 0.5 percent of the beam current.

In the fourth step, CEX interactions between beam ions and facility background neutrals were accounted for. CEX depletes lower-charge-state species more than higher-charge-state species, causing the ExB probe to read more higher-charge-state species than when in the vacuum of space. This effect is especially prominent for high-power thruster tests. The CEX model used to correct the ExB probe data is described in Shastry's work (Ref. 12). The model describes the effect of CEX as a set of attenuation factors that diminishes the detected current at the ExB collector. Equations (16) to (18) show the equations used to calculate the attenuation factors (Ref. 12).

$$(J/J_0)_{Xe^+} = \exp(-n_0\sigma_1 z), \quad \sigma_1 = 87.3 - 13.6\ \log(V_1) \tag{16}$$

$$(J/J_0)_{Xe^{2+}} = \exp(-n_0\sigma_2 z), \quad \sigma_2 = 45.7 - 8.9\ \log(2V_2) \tag{17}$$

$$(J/J_0)_{Xe^{3+}} = \exp(-n_0\sigma_3 z), \quad \sigma_3 = 16.9 - 3.0\ \log(3V_3) \tag{18}$$

Where J is the recorded current density at distance z away from the thruster exit plane, J_0 is the current density that would have been recorded at the thruster exit plane, and n_0 is the average background neutral density. The numerical formulas for the CEX cross-sections, σ_1, σ_2, and σ_3, are given in units of $Å^2$ (10^{-20} m^2). The ion energy per charge, V_1, V_2, and V_3 for Xe^+, Xe^{2+}, and Xe^{3+}, respectively, are assumed to be equal to the average ion energy per charge as measured by the RPA. The value of n_0 is calculated by converting the average of the pressure measurement from four ion gauges. Two of these gauges were located on the chamber wall at the same axial position as the farfield probe tower, one of the gauges was next to the thrust stand, and the last of the gauges was on the chamber wall at an axial location close to the thruster. Note that one can assume the ion energy per charge is equal to the discharge voltage for the purpose of these calculations. Doing so removes the dependence of the ExB probe analysis on the RPA, though with a small increase in uncertainty. See Shastry's work for an estimate of this uncertainty (Ref. 12).

The uncertainty in the charge utilization as calculated from Equation (7) is no more than 0.5 percent. This value is small because the charge utilization is very insensitive to the values of the current fractions. For the 300M, the charge utilization varied from 0.975 to 0.984. For the 300MS, the charge utilization varied from 0.965 to 0.973.

ExB probe data is also used to calculate the α_m term in the mass utilization. Total uncertainty of the mass utilization will be discussed in Section VI; this paragraph will focus on the uncertainty in α_m. Based on the equations derived in the appendix, the average velocity resolution of the ExB probe was 2.7 percent. This value is higher for ions with higher energy per charge and is no more than 4.0 percent for the detectable ion populations with the highest energy per charge. This resolution is sufficiently fine so that the aforementioned ExB probe analysis method is applicable. The ExB probe resolution primarily affected broadening of the measured VDF and has minimal effect on the current fractions. For the 300M, the uncertainty in the current fraction is expected to be dominated by the uncertainty in the average background neutral density measured by the ion gauges. For the 300MS, additional uncertainty is introduced by the strong overlap between charged species peaks. This added uncertainty arises from not being certain about whether the analysis program really only captured contributions from one charged species at a time. For now we will focus on the uncertainty in the ion gauge measurements. The ion gauges are nominally 6 percent accurate. However, they only measured the neutral density in their immediate vicinity. Factors like conductance losses and un-compensated temperature effects on the

electronics are expected to raise the uncertainty of the neutral density measurement to ~15 percent. Substituting in a ±15 percent neutral density uncertainty into the CEX correction formula yielded average uncertainties of ±0.034, ±0.024, and ±0.011 for the Xe^{+}, Xe^{2+}, and Xe^{3+} current fractions, respectively. The corresponding average uncertainty for α_m is ~2 percent. Since much is still not known about the strong overlap between peaks found in the ExB probe traces of the 300MS, the uncertainty in α_m for the 300MS will be tentatively set to twice that of the 300M. Thus, the uncertainty in α_m is 2 percent for the 300M and 4 percent for the 300MS.

B. ExB Probe Results and Comparisons

Figure 12 shows example ExB probe traces from the same reference point (400 V, 20 kW) for the 300M and 300MS. This figure illustrates a common characteristic of ExB probe traces from the 300MS and 300MS-2; there is strong overlap between the different charged species, to the point that the multiply-charged peaks appear to merge into a single large structure. Generally speaking, this overlap trend is strongest for the lower voltage and higher power operating points. Figure 13 illustrates the change in ExB probe trace with discharge voltage for the 300MS. Figure 14 illustrates the change in ExB probe trace with discharge power for the 300MS.

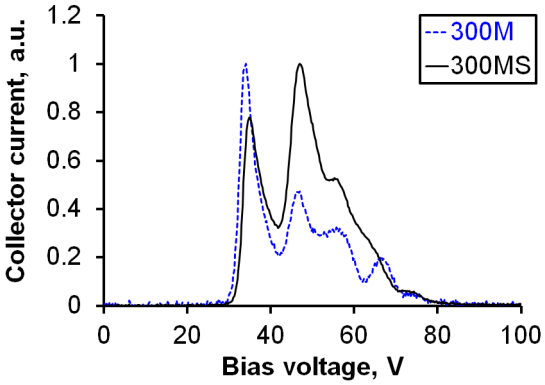

Figure 12.—Comparison of ExB probe traces for the 300M and 300MS at 400 V, 20 kW.

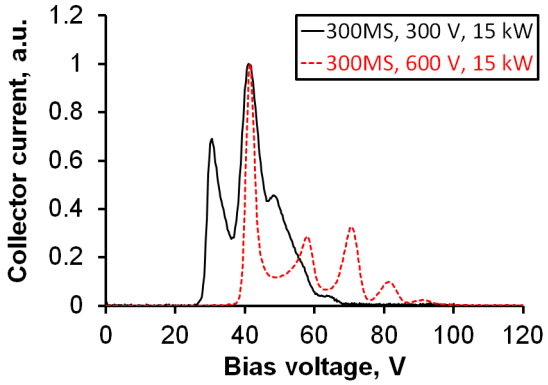

Figure 13.—Comparison of ExB probe traces for the 300MS at 300 and 600 V, 15 kW.

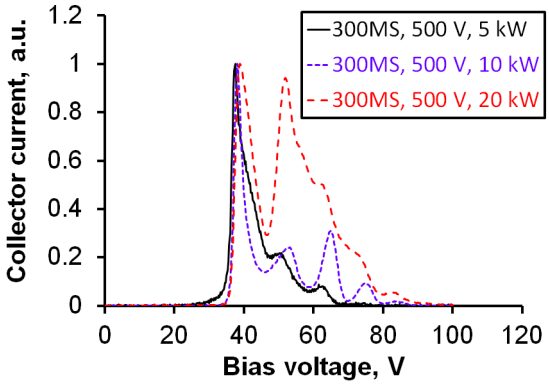

Figure 14.—Comparison of ExB probe traces for the 300MS at 500 V, 5, 10, and 20 kW.

Table 2 summarizes the results of the ExB probe analyses for the 300M and 300MS across the eight reference points. Results for the 300MS-2 were almost identical to the 300MS and will not be tabulated separately. The table shows the Xe^{2+} and Xe^{3+} current fractions. The sum of the current fractions Xe^{+}, Xe^{2+}, and Xe^{3+} is 1. Also shown are the average charge state, α_m, and charge utilization efficiency. The average charge state is calculated using Equation (19).

$$\overline{Z} = \sum_{k} Z_k \zeta_k \tag{19}$$

As with the RPA and Langmuir probe data, averages and standard deviations are shown to aid the reader in comparing the 300M to the 300MS.

Table 2 shows that the 300MS is producing ~70 percent more multiply charged particles than the 300M on the average. This rise in multiply charged species has a much more prominent effect on the value of α_m than on the charge utilization efficiency. The low magnitude of the standard deviation shows that the difference in α_m between the 300M and 300MS is not a statistical fluke. While Table 2 shows the average trends across thrusters, detailed trends are difficult to visualize from Table 2. Figure 15 shows a plot of the average charge state as a function of the discharge current. Since the channel cross section (upstream of the chamfers) was kept the same between the 300M and 300MS, the discharge current is proportional to the current density. Note that this figure is augmented with data from operating points beyond the eight reference points. A rather interesting trend can be seen in this figure. Whereas the

TABLE 2.—SUMMARY OF CHARGE UTILIZATION AND A_M ANALYSES

		Current fraction, Xe^{2+}		Current fraction, Xe^{3+}		Average charge state		α_m		Charge utilization efficiency	
Disch. voltage, V	Disch. power, kW	300M	300MS	300M	300MS	300M	300MS	300M	300MS	300M	300MS
300	10	0.18	0.34	0.04	0.05	1.097	1.195	0.884	0.800	0.980	0.971
300	15	0.24	0.31	0.03	0.08	1.125	1.201	0.858	0.793	0.977	0.968
400	10	0.21	0.33	0.05	0.03	1.122	1.181	0.861	0.811	0.976	0.973
400	15	0.19	0.32	0.06	0.07	1.116	1.205	0.865	0.789	0.976	0.968
400	20	0.18	0.32	0.05	0.09	1.102	1.214	0.878	0.781	0.978	0.967
500	10	0.22	0.27	0.06	0.12	1.134	1.207	0.851	0.786	0.975	0.965
500	15	0.19	0.31	0.05	0.06	1.115	1.187	0.867	0.805	0.977	0.970
500	20	0.20	0.33	0.06	0.09	1.123	1.222	0.858	0.776	0.975	0.967
Average:		0.20	0.32	0.05	0.07	1.117	1.201	0.865	0.793	0.977	0.969
Std. dev.:		-------	------	-----	-----	-----	-----	0.011	0.012	0.002	0.003

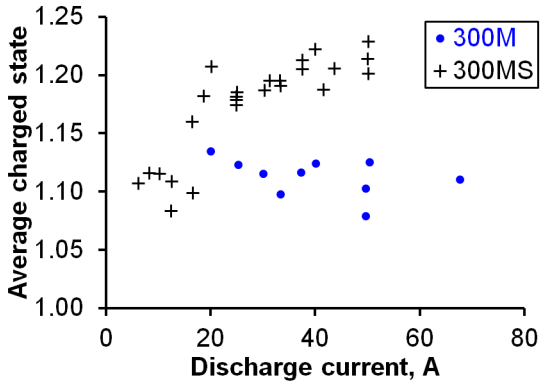

Figure 15.—Average charge state as a function of discharge current for the 300M and 300MS.

average charged state of the 300M remained comparatively constant (to within ±0.03), the same of the 300MS increase quite noticeably with discharge current (and current density). This rise is most rapid at lower discharge current and tapers off at higher discharge current. The change in multiply charged species content is one of the biggest differences between the 300M and 300MS.

VI. Faraday Probe Analysis

A. Analysis Method

Faraday probe data are used to calculate the plume divergence angle and the total ion beam current. The cosine of the momentum-weighted plume divergence angle is defined as the average axial velocity of the particles divided by the average total velocity of the particles. However, momentum-weighted divergence angle is difficult to measure. The typical approach is to measure the charge-weighted divergence angle, which is approximately equal to the momentum-weighted divergence angle if the current fraction is roughly constant across the interrogated domain. For a polarly-swept probe, Equation (20) can be used to calculate the charge-weighted divergence angle.

$$< \cos\ \delta >= \frac{2\pi R_{FP}^{\ 2} \int_0^{\pi/2} j(\theta)\ \cos\theta \sin\theta\, d\theta}{2\pi R_{FP}^{\ 2} \int_0^{\pi/2} j(\theta)\ \sin\theta\, d\theta} \tag{20}$$

Where δ is the charged-weighted divergence angle, θ is the polar angle and is equal to 0° for particles traveling parallel to the firing axis, and $j(\theta)$ is the ion current density as a function of the polar angle. R_{FP} is the distance from the Faraday probe collector to the thruster center at the exit plane and is constant for a polarly-swept probe. Note the denominator is equal to the total ion beam current.

For a nude Faraday probe with a guard ring like the one used in this study, the effective collector area is not exactly equal to the collector frontal surface area. Current that enters the gap between the collector and the guard ring can be collected by the side surfaces of the collector (Ref. 28). According to work by Brown, the current entering the gap is collected by the collector and the guard ring in ratio proportional to the ratio of exposed gap area (Ref. 28). For the probe design used in the present study, the area inside the gap is dominated by area connected to the guard ring (Fig. 7). However there is enough area connected to the collector that some level of correction is needed. Note that only the part of the gap with direct exposure to the incoming ion beam is used in the gap area calculation. Using the approach recommended by Brown, the effective collection area is ~4 percent greater than the collector frontal area. The effective collection area is used for all Faraday probe analysis.

Much like in ExB probe data analysis, CEX is a factor in Faraday probe data analysis. However, whereas CEX is an attenuating factor for ExB probe data, it is a re-distributing factor for Faraday probe data. This is because CEX ions have a different trajectory than the ion it is born from and will tend to show up in the wings of a Faraday probe trace. The region considered the “wings” of a Faraday probe trace can be seen in Figure 16 as the region outside of the two outermost dashed vertical lines. An ExB probe does not see CEX ions because of a combination of small acceptance angle and a tendency to de-emphasize low speed ions. The ExB filter resolution has a dependence on the square of the particle speed and CEX ions have only a small fraction of the speed of beam ions. The best way to correct for the re-distributing behavior of CEX on Faraday probe traces is to take data at multiple distances and facility background pressures (Ref. 28). This could not be carried out for the present study due to space constraints. Instead, an extrapolated-wing approach was used to remove the parts of the trace that are believed to be dominated by re-distributed CEX ions. The extrapolated-wing approach begins by plotting the ion current density on a semi-log scale. Exponential curve-fits are then performed on the data from a polar angle of 10° to 25°. The curve-fit result is then extrapolated to 90°. Note an exponential function of

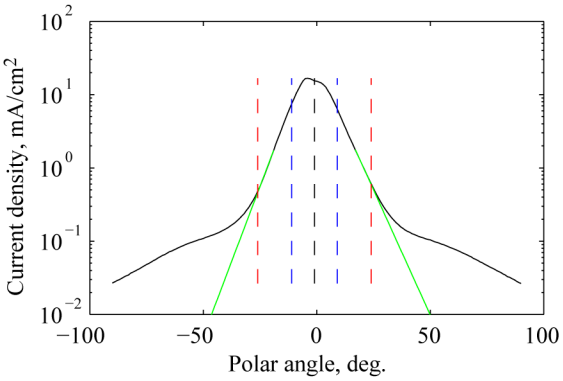

Figure 16.—Illustration of the extrapolated-wing method for analyzing Faraday probe data.

TABLE 3.—SUMMARY OF SEE DATA FOR XENON ION BOMBARDMENT OF MOLYBDENUM (REFS. 32 AND 33)

Bombarding particle	SEE yield of molybdenum
Xe^+	0.022
Xe^{2+}	0.20
Xe^{3+}	0.70

the polar angle shows up as straight lines on the semi-log plot. Figure 16 shows a graphical representation of the extrapolated-wing method. The black solid line is the raw data. The dashed vertical line in the middle is the center of the trace (θ is not quite equal to 0° here due to a minor mis-alignment in the physical setup). The left two and right two dashed vertical lines indicate the boundary for the data used to perform the curve-fit on the respective side. The light green solid lines represent the curve-fit results.

In past studies, low secondary electron emission (SEE) yield materials like molybdenum and tungsten have been used for the collector (Refs. 29 to 31). Secondary electrons born on a negatively biased probe will accelerate away from the probe. This effect adds extra current to the probe measurement that is indistinguishable from the collected ion current. By selecting a low SEE yield material, researchers had believed that the effect of SEE is negligible and can be ignored. While singly-charged xenon-induced SEE yield for molybdenum and tungsten are indeed negligible (0.013 to 0.022), the doubly-charged xenon-induced SEE yield are roughly 10 times higher than the singly-charged yield, and the triply-charged SEE yield are roughly 35 times higher than the singly-charged yield (Refs. 32 to 34). Furthermore, Hagstrum discovered that metastable singly-charged xenon induces roughly the same SEE yield as doubly-charged xenon (Ref. 35). Thus, as long as the plume of the thruster is composed of mostly ground-state singly-charged xenon ions, the assumption of negligible SEE effect holds.

During the present testing, the assumption of negligible SEE effect was discovered to not hold. The material used for the present study is molybdenum, which is considered a low SEE yield material. The reason SEE effects are not negligible is because high-power Hall thrusters appear to produce 20 to 40 percent doubly- and triply-charged ions by current fraction. Combined with the high SEE yield associated with bombardment by higher charge ions, the effect of SEE can be non-negligible. To correct for SEE effects on the Faraday probe measurement, we turn to data published by Hagstrum. Table 3 summarizes the SEE yield values used in the data analysis of the present study. The singly-charged and doubly-charged xenon-induced yields are averages of the SEE yield data for ion energies in the range of 200 to 800 eV in Hagstrum's 1956 work on molybdenum (Ref. 33). For both of these parameters, the value measured by Hagstrum varied by no more than 10 percent of the listed average. A published value for the triply-charged xenon-induced yield of molybdenum could not be found. The value in Table 3 is a projected value based on the similarity in yield between tungsten and molybdenum. The ratio of triply-charged induced yield to doubly-charged induced yield for tungsten is 3.5, so the yield for molybdenum is projected to be 3.5 * 0.2, or 0.7 (Ref. 32).

Equation (21) shows the relationship between the actual ion current density and the ion current density measured by the Faraday probe due to SEE effect.

$$\frac{J}{J_{FP}} = \frac{1}{1 + \sum_{k} \frac{\Omega_k \gamma_k}{Z_k}} \tag{21}$$

Where J is the actual ion current density, J_{FP} is the current density measured by a nude Faraday probe, and γ_k is the SEE yield in number of electrons per ion associated with bombardment by the k-th species. For the present study, the ion current density measured by the nude Faraday probe is 4 to 7 percent higher than the actual current density. The amount of metastable singly-charged ions is assumed to be negligible. This assumption is an extrapolation from controlled ion beam work done by Hagstrum (Ref. 35). In his experiment, Hagstrum varied the energy of the electrons used to generate his singly-charged ion beam from 10 to 70 eV. The SEE yield he measured jumped quickly up from 0.022 to 0.025 when the electron energy was ramped up from 25 to 30 eV, and then plateaued out at 0.025 all the way up to 70 eV. While the Hall thruster ionization zone and an ion beam discharge chamber are not exactly the same they do share many of the same operating principles, including a reliance on impact bombardment ionization. Since the amount of metastable ions was so small that the SEE yield increased by only 0.003 for Hagstrum's experiment, we assumed the effect will be of similar magnitude in a Hall thruster and is therefore negligible.

The Faraday probe data is used in the calculation of several efficiency factors, the uncertainties of each which will now be treated. For the divergence efficiency, the important sources of uncertainty include background CEX effects and SEE effects. Based on prior work by Brown, Faraday probe data taken at 5 MCD away from the thruster should have an uncertainty of no more than 2 percent for the facility background pressure found during the present study (Ref. 28). However, Brown's work was done on a lower power thruster (nominal 6 kW) compared to the 300M and with a correspondingly shorter distance between the probe and the thruster. We estimate the uncertainty associated with CEX to be ~3 percent based on the extra distance between the probe and thruster. The effect of SEE on the uncertainty of the divergence efficiency is more difficult to calculate due to lack of prior experience. However, as long as the current fraction only undergoes small changes as a function of polar angle, the overall effect will be small. This is because SEE represents a relatively small correction to the local current density, so small changes to a small correction should be negligible. Thus, the overall uncertainty in the divergence efficiency is estimated to be 3 percent.

The uncertainty in the current utilization is primarily influenced by uncertainties associated with calculation of the effective collector area, CEX effects, and SEE effects. The effective collector area is expected to be accurate to ~1 percent based on different ways in which the gap current can be distributed between the collector and the guard ring. The use of the extrapolated-wing approach should remove much of the uncertainty associated with the CEX effect, but without additional knowledge about how much uncertainty is removed, we will assign the same 3 percent uncertainty here that was assigned for the divergence efficiency. The uncertainty in the SEE calculation is tricky to estimate because it depends on the uncertainty of the current fractions calculated from the ExB probe data. Substituting in uncertainties in the current fractions previously calculated into the SEE correction equation (Eq. (21)), the uncertainty in the beam current due SEE correction is 1 percent. The total uncertainty in the current utilization, calculated from standard error propagation, is 3.3 percent.

The uncertainty in the mass utilization is dominated by the uncertainty in the measured anode mass flow rate, the total beam current, and the current fraction-dependent factor, α_m. The mass flow rate measurement has an instrumentation uncertainty of ~1 percent. The uncertainty in the total beam current is the same as the uncertainty in the current utilization (3.3 percent). The uncertainty in α_m, which is calculated from the current fractions, is dominated by uncertainty in the average background pressure and

effect of overlap between ExB probe peaks. The uncertainty in α_m was calculated in the preceding section to be 2 percent for the 300M and 4 percent for the 300MS. The total uncertainty, calculated from standard error propagation, in the mass utilization is 4 percent for the 300M and 5.3 percent for the 300MS.

B. Faraday Probe Results and Comparisons

Figure 17 shows example Faraday probe traces from the same reference point (400 V, 20 kW) for the 300M and 300MS. The two traces are normalized by the peak probe current to better illustrate the difference in the shape of the traces. This figure illustrates a common trend seen across the reference points; the current density distribution, measured by the Faraday probe, is generally wider for the 300M than for the 300MS.

Tables 4 and 5 summarize the results of the Faraday probe analyses across the eight reference points for divergence and current utilization efficiencies, respectively. Table 4 quantifies the degrees by which the divergence of the 300MS and 300MS-2 are greater than the 300M. On the average, the divergence of the 300MS is ~2.5° greater than that of the 300M, which translates to ~2.5 percent lower divergence efficiency. For the 300MS versus the 300MS-2, there is practically no difference in divergence. Table 5 shows a small difference in current utilization efficiency between the three thruster versions. However, given that the uncertainty in current utilization measurement is bigger than this difference, part of the difference may not be real.

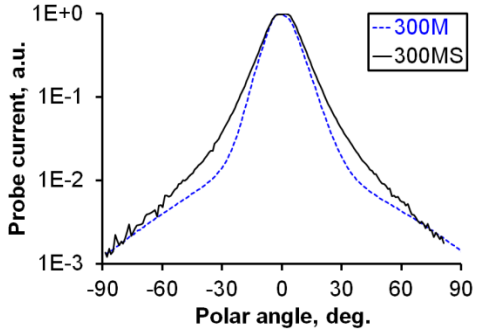

Figure 17.—Comparison of Faraday probe traces for the 300M and 300MS at 400 V, 20 kW.

TABLE 4.—SUMMARY OF DIVERGENCE ANALYSIS

		Divergence angle, degree			Divergence efficiency		
Disch. voltage, V	Disch. power, kW	300M	300MS	300MS-2	300M	300MS	300MS-2
300	10	15.1	20.5	21.0	0.932	0.878	0.871
300	15	18.4	19.7	20.6	0.901	0.887	0.877
400	10	14.9	17.3	16.8	0.934	0.912	0.917
400	15	14.6	17.3	17.2	0.937	0.911	0.913
400	20	14.4	18.4	18.5	0.938	0.900	0.899
500	10	15.3	14.8	15.9	0.931	0.935	0.925
500	15	15.2	16.6	16.4	0.931	0.919	0.921
500	20	14.7	17.9	18.2	0.936	0.906	0.903
Average:		15.3	17.8	18.1	0.930	0.906	0.903
Std. dev.:		1.3	1.8	1.9	0.012	0.018	0.020

TABLE 5.—SUMMARY OF CURRENT UTILIZATION ANALYSIS

		SEE correction factor			Beam current, A			Current utilization efficiency		
Disch. voltage, V	Disch. power, kW	300M	300MS	300MS-2	300M	300MS	300MS-2	300M	300MS	300MS-2
300	10	0.958	0.945	0.946	26.2	26.9	28.0	0.783	0.807	0.834
300	15	0.954	0.941	0.942	39.7	39.5	41.9	0.786	0.787	0.823
400	10	0.953	0.948	0.947	20.2	20.8	20.9	0.796	0.833	0.832
400	15	0.953	0.941	0.941	30.0	30.8	30.8	0.799	0.818	0.822
400	20	0.955	0.938	0.941	39.3	40.3	40.8	0.790	0.806	0.820
500	10	0.951	0.936	0.939	16.5	16.4	17.2	0.817	0.811	0.835
500	15	0.954	0.944	0.944	24.4	25.1	25.0	0.809	0.827	0.831
500	20	0.952	0.938	0.942	32.3	33.0	33.5	0.802	0.826	0.836
	Average:	-----	-----	-----	-----	-----	-----	0.798	0.814	0.829
	Std. dev.:	-----	-----	-----	-----	-----	-----	0.012	0.015	0.006

TABLE 6.—SUMMARY OF MASS UTILIZATION ANALYSIS

		Anode mass flow rate, mg/s			α_m			Mass utilization efficiency		
Disch. voltage, V	Disch. power, kW	300M	300MS	300MS-2	300M	300MS	300MS-2	300M	300MS	300MS-2
300	10	32.3	29.3	29.3	0.884	0.800	0.802	0.976	1.000	1.044
300	15	42.0	40.0	40.0	0.858	0.793	0.791	1.102	1.066	1.128
400	10	25.3	23.8	23.8	0.861	0.811	0.806	0.938	0.968	0.963
400	15	34.9	33.2	33.2	0.865	0.789	0.789	1.010	0.997	0.999
400	20	43.7	40.9	40.9	0.878	0.781	0.795	1.076	1.048	1.078
500	10	20.7	20.4	20.4	0.851	0.786	0.799	0.924	0.858	0.917
500	15	29.1	27.4	27.4	0.867	0.805	0.802	0.991	1.005	0.998
500	20	36.4	34.2	34.2	0.858	0.776	0.797	1.037	1.021	1.065
	Average:	-----	-----	-----	-----	-----	-----	1.007	0.995	1.024
	Std. dev.:	-----	-----	-----	-----	-----	-----	0.063	0.063	0.068

Table 6 summarizes the mass utilization analysis, which depends strongly on both the ExB probe and the Faraday probe analyses. Note that the average of the mass utilization is very close to unity and individual entries may not be physical. On the other hand, earlier calculations showed that the mass utilization has the highest uncertainty of all the efficiency factors. Error in the mass utilization in one direction could be offset by error in another direction in the other efficiency factors. Instead of artificially capping the mass utilization at unity and thereby introducing systematic error, they will be left as they are for the overall efficiency analysis. Additionally, the anode mass flow rate indicates that for a given discharge current, the 300MS used less propellant than the 300M. One possible explanation is that the higher average charge state of the 300MS led to a higher current to mass ratio.

VII. Results and Discussions

Before we proceed to the overall efficiency analysis, the associated uncertainties will be treated. The uncertainty in the anode efficiency as calculated by Equation (1) from the measured thrust is dominated by the uncertainty in the thrust and is 4 percent when calculated via standard error propagation. The total uncertainty in η_a calculated via Equation (2) depends on the uncertainties associated with each of the 5 efficiency factors. Using standard error propagation, the total uncertainty in anode efficiency calculated from the phenomenological efficiency model is 6 percent for the 300M and 7 percent for the 300MS.

We are now ready to study the full physical picture of the 300M, 300MS, and 300MS-2. Since the previous sections have shown how similar the performance of the 300MS-2 is compared to the 300MS, it will not be listed separately. Results and trends shown in this section that pertain to the 300MS also pertain to the 300MS-2. Tables 7 and 8 shows the thrusts and the various efficiency factors calculated during the present study for the 300M and 300MS, respectively. The probe-derived η_a refers to the anode efficiency derived from the use of probe data with the phenomenological model (Eqs. (2) to (7)). The thrust-derived η_a refers to the anode efficiency calculated from thrust measurement via Equation (1).

Tables 7 and 8 show several interesting trends. On the average, the 300MS data shows ~2 percent higher voltage utilization efficiency, ~2.5 percent lower divergence efficiency, and ~1.5 percent higher current utilization efficiency than the 300M data. Although the 300MS produced quite a bit more multiply-charged particles in comparison to the 300M the absolute quantity is fairly modest. Since the charge utilization efficiency equation is largely insensitive to differences of such a modest magnitude, the difference in the charge utilization is less than 1 percent. The two thrusters have roughly the same values in mass utilization efficiencies to within the measurement uncertainties. The anode efficiency calculated from the probe data is nearly identical on the average, though values for individual reference points vary by up to ~6 percent. This variation is similar in magnitude to the uncertainty in the anode efficiency derived from probe data and is likely dominated by uncertainty in the mass utilization. Tables 7 and 8 also show that the anode efficiency calculated from the thrust is, on the average, nearly identical between the 300M and 300MS; the values for individual reference points differ by up to ~2 percent. From the two different methods for calculating the anode efficiency, one can conclude that the NASA-300MS had roughly the same discharge performance as the NASA-300M to within the measurement uncertainties. One can also conclude that the ~6 percent variation in anode efficiency calculated from probe data is likely due to uncertainties in the probe data.

TABLE 7.—SUMMARY OF THRUST MEASUREMENT AND EFFICIENCY ANALYSIS FOR THE 300M

Disch. voltage, V	Disch. power, kW	Thrust, mN	η_v	η_q	η_d	η_b	η_m	Probe-derived, η_a	Thrust-derived, η_a	Difference
300	10	652	0.926	0.980	0.932	0.783	0.976	0.647	0.654	–0.008
300	15	912	0.934	0.977	0.901	0.786	1.102	0.713	0.651	0.061
400	10	581	0.942	0.976	0.934	0.796	0.938	0.641	0.657	–0.017
400	15	852	0.940	0.976	0.937	0.799	1.010	0.694	0.692	0.002
400	20	1099	0.943	0.978	0.938	0.790	1.076	0.736	0.693	0.043
500	10	528	0.962	0.975	0.931	0.817	0.924	0.659	0.668	–0.009
500	15	770	0.942	0.977	0.931	0.809	0.991	0.687	0.673	0.014
500	20	1004	0.959	0.975	0.936	0.802	1.037	0.728	0.686	0.042
	Average:	----	0.944	0.977	0.930	0.798	1.007	0.688	0.672	0.016
	Std. dev.:	----	0.012	0.002	0.012	0.012	0.063	0.037	0.017	0.029

TABLE 8.—SUMMARY OF THRUST MEASUREMENT AND EFFICIENCY ANALYSIS FOR THE 300MS

Disch. voltage, V	Disch. power, kW	Thrust, mN	η_v	η_q	η_d	η_b	η_m	Probe-derived, η_a	Thrust-derived, η_a	Difference
300	10	615	0.947	0.971	0.878	0.807	1.000	0.651	0.646	0.005
300	15	883	0.935	0.968	0.887	0.787	1.066	0.674	0.646	0.028
400	10	578	0.972	0.973	0.912	0.833	0.968	0.695	0.700	–0.005
400	15	832	0.961	0.968	0.911	0.818	0.997	0.691	0.693	–0.002
400	20	1067	0.974	0.967	0.900	0.806	1.048	0.716	0.694	0.022
500	10	515	0.946	0.965	0.935	0.811	0.858	0.594	0.644	–0.051
500	15	755	0.980	0.970	0.919	0.827	1.005	0.726	0.685	0.041
500	20	978	0.981	0.967	0.906	0.826	1.021	0.724	0.700	0.024
	Average:	---	0.962	0.969	0.906	0.814	0.995	0.684	0.676	0.008
	Std. dev.:	---	0.017	0.003	0.018	0.015	0.063	0.045	0.026	0.029

In terms of the fidelity of the efficiency analysis, Tables 7 and 8 show that the combination of the phenomenological model with the data analysis methods and probe design presented in this paper performed very well. On the average, the anode efficiency calculated from probe data matched the anode efficiency calculated from the thrust to within 2 percent. With that said, values for individual reference points were up to 6 percent off indicating possible room for improvement. In statistical terms, the efficiency analysis was very accurate but only moderately precise.

Figure 18 shows a plot of the voltage utilization efficiency as a function of discharge voltage. For a typical Hall thruster, like the 300M, the voltage utilization efficiency increases with discharge voltage. Since the portion of the voltage used by the thruster to draw electrons out of the cathode and the anode sheath drop tends to be relatively constant compared to the change in discharge voltage, thrusters operating at higher discharge voltage are able to allocate more of that voltage drop to accelerating the ions. From this figure, one can see that the voltage utilization efficiency of the 300MS and 300MS-2 display the same behavior.

Figure 19 shows a plot of the divergence efficiency as a function of discharge voltage. For a typical Hall thruster, like the 300M, the divergence efficiency typically rises with the discharge voltage. One hypothesis is that the forces that are responsible for the radial component of the ion velocity (neutral thermal drift, ambipolar field, radial sheath drop, CEX) are relatively constant with rising discharge voltage. Since the accelerating electric field is mostly axial, the ratio of axial to radial ion velocity components rises with the discharge voltage. This trend gives rise to a more focused plasma plume at higher discharge voltage, which leads to a higher divergence efficiency. From this figure, one can see that the divergence efficiency of the 300MS and 300MS-2 display the same trend.

The charge and current utilization efficiencies are largely constant and will not be plotted. Charge utilization is largely constant due to the general insensitivity of the charge utilization equation to current fractions of the multiply-charged species. The invariance of the current utilization with operating conditions have been seen in past work (Refs. 14 and 16). The exact value of current utilization is related to electron mobility and is an ongoing area of research. Since the value of the current utilization is largely constant for both the 300M and 300MS and are roughly equal, the same transport mechanisms are likely to apply for both thrusters.

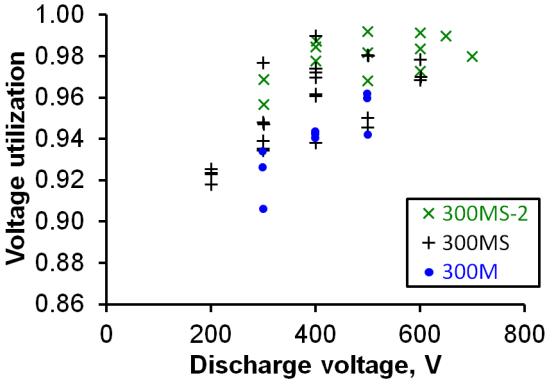

Figure 18.—Divergence efficiency as a function of the discharge voltage.

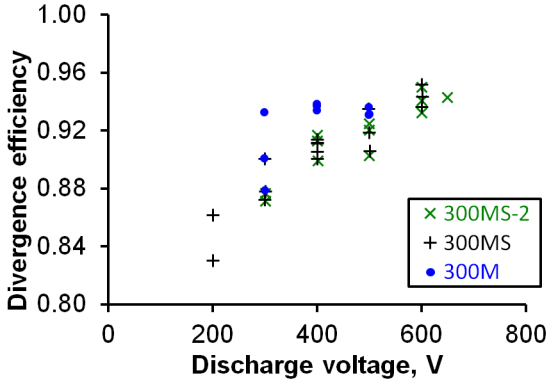

Figure 19.—Mass utilization efficiency as a function of the discharge current.

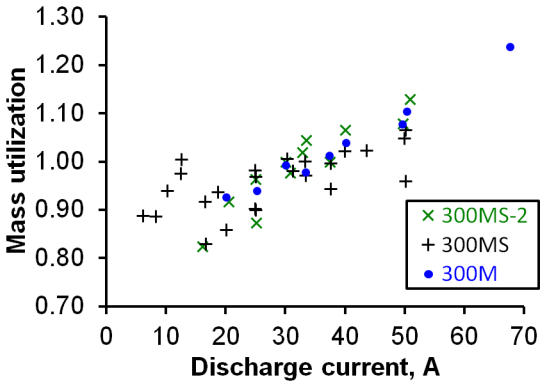

Figure 20.—Mass utilization efficiency as a function of the discharge current.

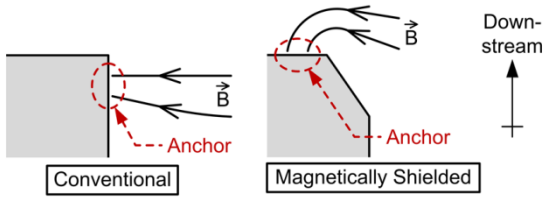

Figure 21.—Illustration of the anchor locations for the magnetic field of conventional and magnetically-shielded Hall thrusters.

Figure 20 shows a plot of the mass utilization efficiency as a function of discharge current. For a typical Hall thruster, like the 300M, the mass utilization efficiency typically rises with the discharge current. The reason is that as the discharge current rise so does the current density and the plasma density. Since the ionization rate scales with the electron density, denser plasma means higher ionization rate, which give rise to higher mass utilization. The mass utilization efficiency of the 300MS and 300MS-2 display the same trends. Note that a value of mass utilization above unity is unphysical. There are two potential sources of error that may explain some of the high mass utilization values. As previously mentioned, the mass utilization draws heavily on both the ExB probe measurement and the Faraday probe measurement. Inaccurate accounting of the multiply charged species such as poor handling of the overlap region between charged peaks can give rise to incorrect values of α_m and, by extension, the mass utilization. For the Faraday probe data, the probe may be capturing more CEX than can be removed by the extrapolated-wing method. If data from either (or both) probe(s) have a positive systematic error, the mass utilization and the associated anode efficiency will be too high, which may explain why the probe-derived anode efficiency is ~1 percent higher than the thrust-derived efficiency. With that said, the error being examined here is around the same as or below the uncertainty of the measurements.

From the tables and figures in this section, one can conclude that the NASA-300MS likely operates on the same ionization and acceleration physics as the NASA-300M. The implementation of magnetic shielding did not change the fundamental laws that govern the basic operating principles of the 300M. The performance of the thruster remained largely unchanged. We will now turn to the small differences that have been observed during the present study and possible physical explanations.

Generally speaking, the plume of the 300MS contains more multiply charged species and has a higher divergence than the plume of the 300M. One possible cause for the higher amount of multiply charged species is the presence of higher temperature plasma associated with reduced wall moderation. The key idea behind magnetic shielding is to maintain a layer of low-temperature, low-density plasma at high plasma potential near the channel walls that extend all the way to the thruster exit (Ref. 8). The anchor points of the magnetic lines of force that travel through the bulk plasma are moved out of the channel and onto the front pole where plasma density is much lower (Fig. 21). As a result the wall area effectively "wetted" by the plasma is reduced by orders of magnitude. In a typical Hall thruster, like the 300M, where the lines of force that pass through the bulk plasma terminates in the ceramic discharge channel walls, electron temperature tends be moderated. Ceramics, like boron nitride, have relatively high secondary electron emission coefficients. When high energy electrons from the bulk plasma impact the wall they are preferentially de-energized and secondary lower-energy electrons are released, resulting in a net decrease in the average electron energy. The electron temperature in a typical Hall thruster does not rise much above some wall-material-dependent critical value even as the discharge voltage increases (Refs. 36). Since the wetted area is much reduced with a magnetically shielded thruster, the electron

temperature can rise as seen in more typical plasma discharges that are not moderated. This increase in electron temperature is seen in simulations though not yet confirmed by interior plasma probing (Ref. 8).

Assuming the plasma temperature in a magnetically-shielded thruster is higher than its more typical cousin, the increase in multiply charged species production will result as a natural consequence. The ionization energies for doubly and triply charged xenon are 21.2 and 32.1 eV, respectively. The average electron temperature found in the ionization zone of a typical Hall thruster is 20 to 30 eV (Refs. 7 and 37). For a plasma with such a temperature, even a small rise in average plasma temperature will mean a large increase in the fraction of electrons (in the high energy tail of the electron energy distribution) that have enough energy to produce multiply charged ions via impact-ionization.

A possible explanation for the increased divergence is that, as a consequence of the magnetic shielding topology, the ionization and acceleration zones of the 300MS are further downstream than the 300M. This change in zone locations was previously seen when the H6 was modified for magnetic shielding (Ref. 8). In such a case, ions with radial momentum are less likely to strike the channel walls and more likely to reach the far-field. Indeed, the main purpose of the magnetic shielding concept is to prevent high-energy ions from striking the channel walls. Another possible explanation is that the magnetically shielding topology has small regions, near the anchor points of the line of force, where the electric field is tilted sideways (Fig. 21). These regions of non-axial electric field correspond to low plasma density so the amounts of ions that escape through them are small. The added radial momentum may explain the small rise in plume divergence.

VIII. Conclusion

This paper has presented an in-depth efficiency analysis of the NASA-300M, a 20-kW thruster, and the NASA-300MS, a magnetically shielded version of the 300M. The results of the phenomenological model with combined inputs from the Langmuir probe, RPA, ExB probe, and Faraday probe shows excellent agreement with thrust stand measurements. On the average, the 300MS data shows ~2 percent higher voltage utilization efficiency, ~2.5 percent lower divergence efficiency, and ~1.5 percent higher current utilization efficiency than the 300M data. The two thrusters have roughly the same values in charge and mass utilization efficiencies. The general conclusion is that the 300M and 300MS have very similar performance as measured by the anode efficiency. Further testing with a second configuration of the 300MS with a shortened discharge channel shows essentially identical performance as the 300MS. The data acquired in the present study will greatly benefit the design of a flight-like magnetically-shielded Hall thruster in the 10 to 15 kW class for SEP TDM.

As part of the current study, a new set of integration formulas were derived for ExB probe analysis. Two VDF equation forms were tried as a part of the analysis. The results show excellent consistency with data obtained from both the 300M and the 300MS. The presence of strong overlap between peaks for the ExB probe data of the 300MS is a new phenomenon in the use of ExB probe in a Hall thruster plume environment. New advances may be needed in the area of Hall thruster charged species spectroscopy to keep up with the newly developed magnetic shielding concept.

Another discovery during the current study is the need to account for secondary electron emission effects on the nude Faraday probe even when a low SEE material is used as the collector. The correction factor for SEE effects were found to vary from 4 to 7 percent and must be accounted for if high fidelity results are needed.

Lastly, several physical explanations are provided to explain the increase in multiply charged species and plume divergence found in the 300MS when compared to the 300M. The discharge of the 300MS is speculated to contain higher temperature electrons and is further downstream than the 300M.

Appendix A—Derivation of New Integration Formulas for ExB Probe Analysis

The process for deriving the integration formulas for ExB probe analysis start by relating the current collected by the ExB probe collector to the velocity distribution functions (VDFs) of the various charged species. To accomplish this, the velocity resolution of the ExB probe is derived in terms of various physical and geometrical properties. The results are used to relate the species and current fraction to the VDFs, culminating in the new integration formulas. This appendix will be written in a stand-alone manner.

To figure out the relationship between the species and current fraction and the ExB probe trace we will first look at the physical description of what exactly the ExB probe is collecting at a given plate bias voltage. This is shown in Equations (22) to (24).

$$I_P(V_P) = \sum_j I_{P,j}(V_P) \tag{22}$$

$$I_{P,j}(V_P) = Z_j e A_P n_j \int_{u_0-\Delta u_j}^{u_0+\Delta u_j} u f_j(u)\,du \tag{23}$$

$$u_0 = \frac{E_0}{B_0} = \frac{V_P}{B_0 D_f} \tag{24}$$

Where I_P is ExB probe collector current, V_P is the plate bias voltage, $I_{P,j}$ is the contribution to the measured current by the j-th species, Z_j is the charge state of the j-th species, e is the elementary charge, A_P is the probe entrance area, n_j is the number density of the j-th species, u is particle velocity, u_0 is the particle velocity corresponding to the applied electric and magnetic field magnitude, E_0 and B_0, respectively, as shown in Equation (24), Δu_j is the half-width of the ExB velocity resolution and varies with species, f_j is the velocity distribution function (VDF) of the j-th species, and D_f is the gap between the ExB bias plates.

To continue, we need to derive the relationship between Δu_j and other known constants and variables. The derivation will be carried out for a single species so the subscript j will be dropped temporarily.

Figure 22 shows the design of a generic ExB probe with a drift section. This simplified and exaggerated diagram also represents the ExB probe used for the present study. Starting from the left of the diagram, we have the collimator with a circular entrance orifice of diameter a_1, a circular exit orifice of diameter a_2, and a length of L_c. The particle is injected at the maximum collimator acceptance angle, α, and enters the filter section. The filter section is of length L_f and is sufficiently wide that the particle does not hit the bias plates (grey rectangles). The electric and magnetic fields in the particle path are uniform, perpendicular, and of magnitude E_0 and B_0, respectively. The example particle in this derivation is traveling slightly faster than the filter velocity u_0, which is equal to E_0/B_0. The velocity of the particle is assigned to be $u_0+\Delta u$. Because the particle is slightly too fast, it experiences a net downward acceleration in the filter section and passes into the drift section. The drift section is of length L_d. The particle is just slow enough to pass through the circular orifice of diameter a_3 in the SEE suppression plate. The collector is sufficiently large as to collect all ions passing through the orifice on the SEE suppression plate. In some ExB probe designs, an exit collimator replaces the SEE suppression plate. The diameter of the entrance orifice for the exit collimator would become a_3. Two assumptions will be used in this derivation. One, the acceptance angle is small enough that small angle approximation applies. Two, $\Delta u << u_0$, so the equation can be linearized.

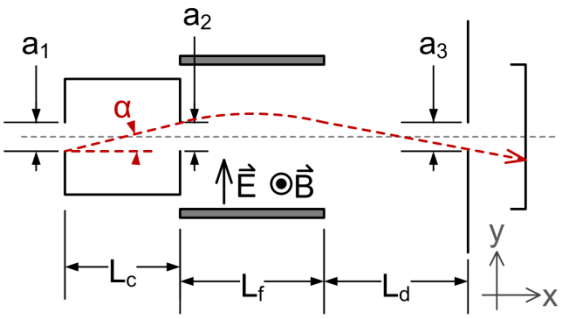

Figure 22.—Simplified diagram of a generic ExB probe with drift section.

Applying the equations of motion to the collimator section, we can obtain Equation (25) for the acceptance angle of the collimator. Note the use of the small angle approximation.

$$\sin\alpha \approx \tan\alpha = \frac{a_1 + a_2}{2L_c} \tag{25}$$

Applying the equations of motion to the filter section, we obtain Equation (26) for the x-axis and Equation (27) for the y-axis. Note the use of the $\Delta u << u_0$ assumption in Equation (26).

$$\tau_f \approx L_f / u_0 \tag{26}$$

$$\Delta y_f = \tfrac{1}{2}\Delta a\,\tau_f^{\,2} + u_0 \sin\alpha\,\tau_f \tag{27}$$

$$\Delta u = -\frac{m}{ZeB_0}\Delta a \tag{28}$$

Where τ_f is the dwell time of the particle in the filter section, Δy_f is the change in y-position of the particle between where it enters and where it exits the filter section, Δa is the net acceleration on the particle due to the velocity of the particle deviating from the filter velocity, m is the mass of the particle, and e is the elementary charge. The relationship between Δu and Δa is derived from force balance in the filter section and shown in Equation (28). Applying the equations of motion to the drift section, we obtain Equation (29) for the x-axis and Equation (30) for the y-axis.

$$\tau_d \approx L_d / u_0 \tag{29}$$

$$\Delta y_d = u_{y,d}\tau_d = \Delta a\,\tau_f\tau_d + u_0 \sin\alpha\,\tau_d \tag{30}$$

where τ_d is the dwell time of the particle in the drift section, Δy_d is the change in y-position of the particle between where it enters and where it exits the drift section, and $u_{y,d}$ is the y-velocity of the particle as it enters the drift section. $u_{y,d}$ is calculated from the equations of motion for the filter section. Next, we note that the total change in the y-position of the particle between where it enters the filter section and where it exits the drift section is equal to the negative of the difference in y-position between the upper lip of the collimator exit and the lower lip of the orifice on the SEE suppression plate. This relationship is expressed in Equation (31).

$$\Delta y_f + \Delta y_d = -\left(\frac{a_2 + a_3}{2}\right) \tag{31}$$

Substituting Equations (25) to (27), (29), and (30) into Equation (31) and re-arranging some terms, we obtain Equation (32). Lastly, substituting Equation (32) into Equation (28), we obtain an expression for the maximum deviation in velocity that a particle can have and still reach the collector.

$$\Delta a = -\left[\frac{a_2 + a_3 + (a_1 + a_2)(L_f + L_d)/L_c}{{L_f}^2 + 2L_d L_f}\right]{u_0}^2 \tag{32}$$

$$\Delta u = \frac{m{u_0}^2}{ZeB_0}\left[\frac{a_2 + a_3 + (a_1 + a_2)(L_f + L_d)/L_c}{{L_f}^2 + 2L_d L_f}\right] \tag{33}$$

Note, if the acceptance angle of the ExB probe is larger than the angle subtended by the plasma source, the angle α is no longer the limiting parameter. Instead, the angle β (Eq. (34)) should be used and the form of Equation (33) changes to Equation (35).

$$\sin\beta \approx \frac{D_{PS}}{2R_{ExB}} \tag{34}$$

$$\Delta u = \frac{m{u_0}^2}{ZeB_0}\left[\frac{a_2 + a_3 + 2\sin\beta(L_f + L_d)}{{L_f}^2 + 2L_d L_f}\right] \tag{35}$$

where D_{PS} is the diameter of the plasma source and R_{ExB} is the distance between the ExB probe and the plasma source. For the probe used in this study, the acceptance angle is sufficiently small that Equation (35) does not apply.

For an ExB probe without a drift section, we can set L_d to 0 in Equation (33), which simplifies into Equation (36).

$$\Delta u = \frac{m{u_0}^2}{ZeB_0}\left[\frac{a_2 + a_3 + (a_1 + a_2) * L_f / L_c}{{L_f}^2}\right] \tag{36}$$

Comparing Equations (36) to (33), we see that the addition of the drift section will generally improve the resolution of the ExB probe. Note that a_1, a_2, a_3, L_c, L_f, L_d, and R_{ExB} are all geometric constants for a given experimental setup. D_{PS} is also typically a constant (though one can never be too careful when generalizing about plasma sources). We can now write a scaling equation for the maximum accepted deviation in velocity of a generic ExB probe, which is shown in Equation (37).

$$\Delta u = \frac{m{u_0}^2}{ZeB_0}G \tag{37}$$

where G is a geometric constant.

Here are some quick observations about the maximum accepted deviation in velocity for an ExB probe. One, the numerator of Equation (37) contains the ion kinetic energy while the denominator contains the ion charge. In other words, Δu scales with the ion energy per charge of the incoming

particles, which is slightly lower than the discharge voltage of a Hall thruster. The implication of this trend for a Hall thruster is that Δu is species-insensitive because all charged species undergo similar voltage drop and have similar ion energy per charge. When calculating ExB probe resolution as a relative percentage, the value for the singly-charged species will always be the biggest. That is because Δu is roughly constant while u_0 increases with species charge.

Two, dividing both sides of Equation (37) by u_0, we obtain Equation (38).

$$\frac{\Delta u}{u_0} = \frac{mu_0}{ZeB_0} G \tag{38}$$

This equation says that for a given charged species, the ExB probe resolution in relative percentage increases with the velocity of the particle. For instance, an ExB probe with a ±2 percent resolution when probing the plume of a 250-V thruster would have a ±4 percent resolution when probing the plume of a 1000-V thruster. The probe resolution in relative percentage scales as the velocity of the particles, which scale as the square root of the accelerating voltage. This is part of the reason why ExB probe traces for ion thruster are typically unable to resolve the VDF of the plume particles. The high accelerating voltage (1000+ V) associated with an ion thruster means Δu will generally be large. The combination of low VDF spread and large Δu means that Δu is generally larger than the VDF spread for an ion thruster. This interesting trend also means that an ExB probe used to interrogate the plume of a Hall thruster operating at high discharge voltage should have tight dimensions to ensure Δu is several times smaller than the width of the ion VDF.

Having related Δu to known constants and variables, we now put back the subscript j in the appropriate places to indicate species-dependence. Mass is normally species dependent; however, Hall thrusters typically operate on a single atomic species so we will use a single atomic mass constant. The result is shown in Equation (39).

$$\Delta u_j = \frac{m{u_0}^2}{Z_j eB_0} G \tag{39}$$

For an ExB probe with good velocity resolution, that is to say $\Delta u_j << u_0$, the integral term in Equation (23) can be approximated as $f_j(u_0)*2\Delta u_j$. Taking the $\Delta u_j << u_0$ approximation and substituting Equation (39) into Equation (23), we arrive at Equation (40).

$$I_{P,j}(V_P) = K_0 {u_0}^3 n_j f_j(u_0), \quad K_0 \equiv \frac{2A_P mG}{B_0} \tag{40}$$

where K_0 is a constant for a given probe design. Further substituting Equation (24) into Equation (40), we arrive at Equation (41).

$$I_{P,j}(V_P) = K_1 n_j {V_P}^3 f_j(K_2 V_P), \quad K_1 \equiv \frac{K_0}{(B_0 D_f)^3}, \quad K_2 = \frac{1}{B_0 D_f} \tag{41}$$

Where K_1 and K_2 are constants for a given probe design. Depending on which VDF form is in use, the associated equation is substituted into f_j, and Equation (41) is fitted to the ExB probe trace to solve for the fitting constant. Note, Equation (13) is the same as Equation (41). The formulas presented so far, though appearing in different forms, matches previously published work (Refs. 12 and 27). It is the formulas to follow that are original and diverge from past work.

To calculate the species fraction and current fraction, we now need the integral equations relating each quantity to the ExB probe collector current. To find the species fraction, we begin by re-arranging the V_P^3 term, then integrating both sides of Equation (41) with respect to V_P from 0 to ∞. Since n_j does not depend on V_P it can go outside the integral. The result is shown in Equation (42). Since the integral of f_j from 0 to ∞ is unity, we can further simplify the result, which is shown in Equation (43).

$$K_1 n_j \int_0^\infty f_j(K_2 V_P)\, dV_P = \int_0^\infty \frac{I_{P,j}(V_P)}{{V_P}^3} dV_P \tag{42}$$

$$n_j = \frac{1}{K_1} \int_0^\infty \frac{I_{P,j}(V_P)}{{V_P}^3} dV_P \tag{43}$$

Equation (43) relates n_j to the ExB probe collector current and can be used to calculate the species fraction. The integration formula for species fraction is shown in Equation (44).

$$\zeta_j \equiv \frac{n_j}{\sum_k n_k} = \frac{\int_0^\infty \frac{I_{P,j}(V_P)}{{V_P}^3} dV_P}{\sum_k \int_0^\infty \frac{I_{P,k}(V_P)}{{V_P}^3} dV_P} \tag{44}$$

To find the current fraction, we begin by relating the current of the j-th species entering the ExB probe, I_j, to the probe collector current. The current of the j-th species is defined in Equation (45). Substituting Equation (24) into Equation (45) yields Equation (46).

$$I_j = Z_j e A_P n_j \int_0^\infty u_0\, f_j(u_0)\, du_0 \tag{45}$$

$$I_j = Z_j e A_P {K_2}^2 n_j \int_0^\infty V_P\, f_j(K_2 V_P)\, dV_P \tag{46}$$

Next, we rearrange Equation (41) by dividing both sides by V_P^2, then integrate both sides with respect to V_P from 0 to ∞ to obtain Equation (47). Substituting Equation (47) into Equation (46) yields Equation (48).

$$n_j \int_0^\infty V_P\, f_j(K_2 V_P)\, dV_P = \frac{1}{K_1} \int_0^\infty \frac{I_{P,j}(V_P)}{{V_P}^2} dV_P \tag{47}$$

$$I_j = \frac{Z_j e A_P {K_2}^2}{K_1} \int_0^\infty \frac{I_{P,j}(V_P)}{{V_P}^2} dV_P \tag{48}$$

Equation (48) relates I_j to the ExB probe collector current and can be used to calculate the current fraction. The integration formula for the current fraction is shown in Equation (49).

$$\Omega_j \equiv \frac{I_j}{\sum_k I_k} = \frac{Z_j \int_0^\infty \frac{I_{P,j}(V_P)}{{V_P}^2} dV_P}{\sum_k Z_k \int_0^\infty \frac{I_{P,k}(V_P)}{{V_P}^2} dV_P} \tag{49}$$

Appendix B—Traditional Versus New Integration Formulas for ExB Probe Analysis

Recall, the traditional approach to analyzing ExB probe data involves calculating either by geometry or by numerical integration the area under the curve, which is assumed to be proportional to the current of the corresponding species entering the probe. The traditional integration formula for the current fraction can be written as Equation (50).

$$\Omega_j \equiv \frac{I_j}{\sum_k I_k} \approx \frac{\int_0^\infty I_{P,j}(V_P)\,dV_P}{\sum_k \int_0^\infty I_{P,k}(V_P)\,dV_P} \tag{50}$$

While Equation (50) is mathematically incorrect, it turns out to be a pretty good approximation of Equation (49) for analyzing the plume of a Hall thruster, especially when the VDF is narrow. To see why this is the case, let us calculate the current fractions for both integration formulas in the limit of very narrow VDFs.

The current fraction calculated from the old (traditional) approach will be labeled with Ω_j^O and the current fraction calculated from the new approach will be labeled with Ω_j^N. Assuming the incoming ion beam is composed of species with very narrow VDFs and all charged species undergo the same voltage drop, Equation (49) can be simplified as shown in Equation (51), and Equation (50) can be simplified as shown in Equation (52).

$$\Omega_j^N = \frac{Z_j \int_0^\infty \frac{I_{P,j}(V_P)}{{V_P}^2}\,dV_P}{\sum_k Z_k \int_0^\infty \frac{I_{P,k}(V_P)}{{V_P}^2}\,dV_P} \xrightarrow[\text{VDF}]{\text{Narrow}} \frac{Z_j n_j \bar{u}_j}{\sum_k Z_k n_k \bar{u}_k} \xrightarrow[V_d]{\text{Same}} \frac{n_j {Z_j}^{3/2}}{\sum_k n_k {Z_k}^{3/2}} \tag{51}$$

$$\Omega_j^O \approx \frac{\int_0^\infty I_{P,j}(V_P)\,dV_P}{\sum_k \int_0^\infty I_{P,k}(V_P)\,dV_P} \xrightarrow[\text{VDF}]{\text{Narrow}} \frac{n_j {\bar{u}_j}^3}{\sum_k n_k {\bar{u}_k}^3} \xrightarrow[V_d]{\text{Same}} \frac{n_j {Z_j}^{3/2}}{\sum_k n_k {Z_k}^{3/2}} \tag{52}$$

The simplified expressions for the two integration approaches are equal. The voltage drop is typically very similar between the charged species, thus any difference in the results between the new and old approaches arise mostly from differences in the way the two approaches account for the spread in the VDF. During the present study, the difference was found to correspond to a change in anode efficiency of only 1 to 2 percent on the average.

References

1. "NASA Exploration Systems Mission Directorate Presentation, Human Space Exploration Summary," http://www.nasa.gov/exploration/new_space_enterprise/home/heft_summary.html, Jan., 2011.
2. Mercer, C.R., et al., "Benefits of Power and Propulsion Technology for a Piloted Electric Vehicle to an Asteroid," *47th AIAA/ASME/SAE/ASEE Joint Propulsion Conference & Exhibit*, AIAA-2011-7252, San Diego, CA, 31 Jul.- 3 Aug., 2011.
3. Capadona, L.A., et al., "Feasibility of Large High-Powered Solar Electric Propulsion Vehicles: Issues and Solutions," *47th AIAA/ASME/SAE/ASEE Joint Propulsion Conference & Exhibit*, AIAA-2011-7251, San Diego, CA, 31 Jul.- 3 Aug., 2011.
4. Brophy, J.R., et al., "300-kW Solar Electric Propulsion System Configuration for Human Exploration of Near-Earth Asteroids," *47th AIAA/ASME/SAE/ASEE Joint Propulsion Conference & Exhibit*, AIAA-2011-5514, San Diego, CA, 31 Jul.- 3 Aug., 2011.
5. Hofer, R.R. and Randolph, T.M., "Mass and Cost Model for Selecting Thruster Size in Electric Propulsion Systems," *47th AIAA/ASME/SAE/ASEE Joint Propulsion Conference & Exhibit*, AIAA-2011-5518, San Diego, CA, 31 Jul.- 3 Aug., 2011.
6. Mikellides, I.G., et al., "Magnetic shielding of the channel walls in a Hall plasma accelerator," *Physics of Plasmas*, vol. 18, no. 3, doi:10.1063/1.3551583, Mar. 8, 2011, pp. 033501.
7. Hofer, R.R., Goebel, D.M., Mikellides, I.G., and Katz, I., "Design of a Laboratory Hall Thruster with Magnetically Shielded Channel Walls, Phase II: Experiments," *48th AIAA/ASME/SAE/ASEE Joint Propulsion Conference & Exhibit*, AIAA-2012-3788, Atlanta, GA, 29 Jul.- 1 Aug., 2012.
8. Mikellides, I.G., Katz, I., Hofer, R.R., and Goebel, D.M., "Design of a Laboratory Hall Thruster with Magnetically Shielded Channel Walls, Phase III: Comparison of Theory with Experiment," *48th AIAA/ASME/SAE/ASEE Joint Propulsion Conference & Exhibit*, AIAA-2012-3789, Atlanta, GA, 29 Jul.- 1 Aug., 2012.
9. Kamhawi, H., Haag, T.W., Jacobson, D.T., and Manzella, D. H., "Performance Evaluation of the NASA-300M 20 kW Hall Effect Thruster," *47th AIAA/ASME/SAE/ASEE Joint Propulsion Conference & Exhibit*, AIAA-2011-5521, San Diego, CA, 31 Jul.- 3 Aug., 2011.
10. Kamhawi, H., et al., "Performance and Thermal Characterization of the 20 kW 300MS Hall Effect Thruster," *33rd International Electric Propulsion Conference*, 2013-444, Washington, DC, 6-10 Oct., 2013.
11. Shastry, R., Huang, W., Haag, T.W., and Kamhawi, H., "Langmuir Probe Measurements within the Discharge Channel of the 20-kW NASA-300M and NASA-300MS Hall Thrusters," *33rd International Electric Propulsion Conference*, 2013-122, Washington, DC, 6-10 Oct., 2013.
12. Shastry, R., Hofer, R.R., Reid, B.M., and Gallimore, A.D., "Method for analyzing ExB probe spectra from Hall thruster plumes," *Review of Scientific Instruments*, vol. 80, no. 6, doi:10.1063/1.3152218, 22 Jun., 2009, pp. 063502.
13. Kim, V., "Main physical features and processes determining the performance of stationary plasma thrusters," *Journal of Propulsion and Power*, vol. 14, no. 5, 1998, pp. 736-743.
14. Hofer, R.R. and Gallimore, A.D., "High-Specific Impulse Hall Thrusters, Part 2: Efficiency Analysis," *Journal of Propulsion and Power*, vol. 22, no. 4, doi:10.2514/1.15954, Jul.-Aug., 2006, pp. 732-740.
15. Brown, D.L., "Investigation of Flow Discharge Voltage Hall Thruster Characteristics and Evaluation of Loss Mechanisms," Ph.D. Dissertation, Aerospace Engineering, University of Michigan, Ann Arbor, MI, 2009.
16. Reid, B.M., "The Influence of Neutral Flow Rate in the Operation of Hall Thrusters," Ph.D. Dissertation, Aerospace Engineering, University of Michigan, Ann Arbor, MI, 2008.
17. Manzella, D.M., "Scaling Hall Thrusters to High Power," Ph.D. Dissertation, Mechanical Engineering, Stanford University, Stanford, CA, 2005.

18. Hofer, R.R., Peterson, P.Y., Gallimore, A.D., and Jankovsky, R.S., "A High Specific Impulse Two-Stage Hall Thruster with Plasma Lens Focusing," *27th International Electric Propulsion Conference*, IEPC-2001-036, Pasadena, CA, 15-19 Oct., 2001.
19. Hofer, R.R. and Gallimore, A.D., "The Role of Magnetic Field Topography in Improving the Performance of High-Voltage Hall Thrusters," *38th AIAA/ASME/SAE/ASEE Joint Propulsion Conference & Exhibit*, AIAA-2002-4111, Indianapolis, IN, 7-10 Jul., 2002.
20. Haag, T.W., "Thrust stand for high-power electric propulsion devices," *Review of Scientific Instruments*, vol. 62, no. 5, doi:10.1063/1.1141998, May, 1991, pp. 1186.
21. Lieberman, M.A. and Lichtenberg, A.J., *Electrostatic Probe Diagnostics*, in *Principles of Plasma Discharges and Materials Processing*, 2nd ed., Ch., doi:10.1002/0471724254, Wiley, New York, 2005, pp. 185-203.
22. Savitzky, A. and Golay, M.J.E., "Smoothing and Differentiation of Data by Simplified Least Squares Procedures," *Analytical Chemistry*, vol. 36, no. 8, doi:10.1021/ac60214a047, Jul., 1964, pp. 1627-1639.
23. Steinier, J., Termonia, Y., and Deltour, J., "Comments on Smoothing and Differentiation of Data by Simplified Least Squares Procedure," *Analytical Chemistry*, vol. 44, no. 11, doi:10.1021/ ac60319a045, Sep., 1972, pp. 1906-1909.
24. Hutchinson, I.H., *Principles of Plasma Diagnostics*, 2nd ed., doi:10.1017/CBO9780511613630, Cambridge University Press, 2002.
25. Beal, B.E., "Clustering of Hall Effect Thrusters for High-Power Electric Propulsion Applications," Ph.D. Dissertation, Aerospace Engineering, University of Michigan, Ann Arbor, MI, 2004.
26. Linnell, J.A., "An Evaluation of Krypton Propellant in Hall Thrusters," Ph.D. Dissertation, Aerospace Engineering, University of Michigan, Ann Arbor, MI, 2007.
27. Kim, S.-W., "Experimental Investigations of Plasma Parameters and Species-Dependent Ion Energy Distribution in the Plasma Exhaust Plume of a Hall Thruster," Ph.D. Dissertation, Aerospace Engineering, University of Michigan, Ann Arbor, MI, 1999.
28. Brown, D.L. and Gallimore, A.D., "Evaluation of Facility Effects on Ion Migration in a Hall Thruster Plume," *Journal of Propulsion and Power*, vol. 27, no. 3, doi:10.2514/1.B34068, May-Jun, 2011, pp. 573-585.
29. Brown, D.L. and Gallimore, A.D., "Evaluation of Ion Collection Area in Faraday probes," *Review of Scientific Instruments*, vol. 81, no. 6, doi:10.1063/1.3449541, 25 Jun., 2010, pp. 063504.
30. Huang, W., Kamhawi, H., and Shastry, R., "Farfield Ion Current Density Measurements before and after the NASA HiVHAc EDU2 Vibration Test," *48th AIAA/ASME/SAE/ASEE Joint Propulsion Conference & Exhibit*, AIAA-2012-4195, Atlanta, GA, 29 Jul.- 1 Aug., 2012.
31. Reid, B.M. and Gallimore, A.D., "Near-field Ion Current Density Measurements of a 6-kW Hall Thruster," *31st International Electric Propulsion Conference*, 2009-124, Ann Arbor, MI, 20-24 Sep., 2009.
32. Hagstrum, H.D., "Auger Ejection of Electrons From Tungsten by Noble Gas Ions," *Physical Review*, vol. 96, no. 2, doi:10.1103/PhysRev.96.325, 15 Oct., 1954, pp. 325-335.
33. Hagstrum, H.D., "Auger Ejection of Electrons from Molybdenum by Noble Gas Ions," *Physical Review*, vol. 104, no. 3, doi:10.1103/PhysRev.104.672, 1 Nov., 1956, pp. 672-683.
34. Hagstrum, H.D., "Auger Ejection of Electrons From Tungsten by Noble Gas Ions," *Physical Review*, vol. 104, no. 2, doi:10.1103/PhysRev.104.317, 15 Oct., 1956, pp. 317-318.
35. Hagstrum, H.D., "Metastable Ions of the Noble Gases," *Physical Review*, vol. 104, no. 2, doi:10.1103/PhysRev.104.309, Sep., 1956, pp. 309-316.
36. Choueiri, E.Y., "Fundamental difference between the two Hall thruster variants," *Physics of Plasmas*, vol. 8, no. 11, doi:10.1063/1.1409344, Nov., 2001, pp. 5025-5033.
37. Reid, B.M. and Gallimore, A.D., "Langmuir Probe Measurements in the Discharge Channel of a 6-kW Hall Thruster," *44th AIAA/ASME/SAE/ASEE Joint Propulsion Conference & Exhibit*, AIAA-2008-4920, Hartford, CT, 21-23 Jul., 2008.